CZECH TECHNICAL UNIVERSITY IN PRAGUE

FACULTY OF NUCLEAR SCIENCES AND PHYSICAL ENGINEERING

Department of Physics

Physics and Technology of Nuclear Fusion

MASTER'S THESIS

Research of a detector for studying high-energy photons generated during laser-plasma interaction.

Zkoumání detektoru vysokoenergetických fotonů vytvořených v průběhu interakce laser-plazma.

Author: Bc. Valeriia Istokskaia
Supervisor: Lorenzo Giuffrida, Ph.D.
Consultants: Ing. Jan Pšikal, Ph.D.
Roberto Versaci, Ph.D.

Prague, 2019

ČESKÉ VYSOKÉ UČENÍ TECHNICKÉ V PRAZE
FAKULTA JADERNÁ A FYZIKÁLNĚ INŽENÝRSKÁ
PRAHA 1 - STARÉ MĚSTO, BŘEHOVÁ 7 - PSČ 115 19

Katedra: fyziky *Akademický rok:* 2018/2019

ZADÁNÍ DIPLOMOVÉ PRÁCE

Student: Bc. Valeriia Istokskaia

Studijní program: Aplikace přírodních věd

Obor: Fyzika a technika termojaderné fúze

Název práce: (česky) Zkoumání detektoru vysokoenergetických fotonů vytvořených v průběhu interakce laser-plazma

Název práce: (anglicky) Research of a detector for studying high-energy photons generated during laser-plasma interaction

Pokyny pro vypracování:

1. Interakce petawattových laserů s pevnolátkovými terči.
2. Generace vysokoenergetických fotonů během interakce petawattového laseru s terčem.
3. Přehled běžné aktivní diagnostiky pro detekci vysokoenergetického záření.
4. Simulace interakce vysokoenergetických fotonů s vícevrstvým elektromagnetickým kalorimetrem pomocí kódu FLUKA.
5. Optimalizace vybraných materiálů a počtu vrstev tohoto detektoru.
6. Vývoj metody pro výpočet teploty záření energetických fotonů na základě dat z detektoru.

Doporučená literatura:

1. G. F. Knoll: Radiation Detection and Measurement, 4th edition, John Wiley & Sons, 2010

2. C. Leroy, P.G. Rancoita: Principles of radiation interaction in matter and detection, 2nd edition, World Scientific, 2009

3. P. Gibbon: Short pulse laser interactions with matter: An introduction, Imperial College Press, London, 2005

4. A. Ferrari, et al. FLUKA: A multi-particle transport code (Program version 2005). No. INFN-TC-05-11, 2005

Jméno a pracoviště vedoucího diplomové práce: Lorenzo Giuffrida, Ph.D., FZÚ AV ČR

Jméno a pracoviště konzultanta:
Ing. Jan Pšikal, Ph.D., KFE FJFI ČVUT

Jméno a pracoviště druhého konzultanta:
Roberto Versaci, Ph.D., FZÚ AV ČR

Datum zadání diplomové práce: 22.10.2018

Termín odevzdání diplomové práce: 06.05.2019

Doba platnosti zadání je dva roky od data zadání.

.....
garant oboru

.....
vedoucí katedry

.....
děkan

ČESKÉ VYSOKÉ UČENÍ TECHNICKÉ V PRAZE
Fakulta jaderná a fyzikálně inženýrská
-1-

V Praze dne 22.10.2018

Prohlášení

Prohlašuji, že jsem svou diplomovou práci vypracovala samostatně a použila jsem pouze podklady (literaturu, projekty, SW atd.) uvedené v přiloženém seznamu.

Nemám závažný důvod proti použití tohoto školního díla ve smyslu §60 Zákona č. 121/2000 Sb., o právu autorském, o právech souvisejících s právem autorským a o změně některých zákonů (autorský zákon).

V Praze dne .....

.....
Bc. Valeriia Istokskaia

Acknowlegement

I would like to express my sincere gratitude to my supervisor Lorenzo Giuffrida, Ph.D. for his guidance, patience and encouragement throughout the work. Furthemore, I would like to thank my consultants Roberto Vercaci, Ph.D. and Ing. Jan Pšikal, Ph.D. for providing me with invaluably constructive criticism and useful suggestions. I am also very grateful to Ing. Vojtěch Stránský for his friendly approach and support on the way.

Bc. Valeriia Istokskaia

Název práce: **Zkoumání detektoru vysokoenergetických fotonů vytvořených v průběhu interakce laser-plazma.**
Autor: Bc. Valeriia Istokskaia
Obor: Fyzika a Technika Termojaderné Fúze
Druh práce: Diplomová práce
Vedoucí práce: Lorenzo Giuffrida, Ph.D., FZÚ AV ČR
Konzultanti: Ing. Jan Pšikal, Ph.D., KFE FJFI ČVUT
Roberto Versaci, Ph.D., FZÚ AV ČR

Abstrakt: Tato práce se zaměřuje na zkoumání nového typu detektoru vysokoenergetických fotonů určeného pro nadcházející experimenty ve výzkumném centru ELI Beamlines. Vzhledem k tomu, že lasery v ELI Beamlines budou charakterizovány ultravysokými výkony a intenzitami (více než 10^{21} W/cm^2), extrémně intenzivní a krátké pulsy energetických fotonů (rtg a gama s teplotou až 50 MeV) budou vyzařovány během interakce těchto laserů s terči. Běžně používaná diagnostika není schopná provádět spektrometrii pulzního fotonového záření v reálném čase, a proto byl vyvíjen nový detektor – elektromagnetický kalorimetr. V ideálním případě takový detektor bude schopen odhadnout teplotu produkovaných fotonů a stanovit jejich energetické rozdělení. Tato práce zahrnuje popis výsledků simulací, které byly provedeny pro návrh kalorimetru pomocí simulačního kódu FLUKA, a možné algoritmy rekonstrukce signálu z detektoru.

Klíčová slova: petawattové lasery, detektor vysokoenergetických fotonů, elektromagnetický kalorimetr, rekonstrukce signálu, fyzika plazmatu

Title of work: **Research of a detector for studying high-energy photons generated during laser-plasma interaction.**
Author: Bc. Valeriia Istokskaia
Specialization: Physics and Technology of Nuclear Fusion
Type of thesis: Master's thesis
Supervisor: Lorenzo Giuffrida, Ph.D., FZÚ AV ČR
Consultants: Ing. Jan Pšikal, Ph.D., KFE FJFI ČVUT
Roberto Versaci, Ph.D., FZÚ AV ČR

Abstract: The thesis focuses on the research of a new type of high-energy photons detector to be used in upcoming experiments in the frame of the ELI Beamlines project. Since lasers with ultra-high peak powers and intensities (more than 10^{21} W/cm^2) will be available at ELI Beamlines, extremely intense and short high-energy photon bursts (with temperature up to 50 MeV) will be emitted during the laser-matter interaction. The currently used diagnostics are not suitable for real-time spectroscopy of such radiation, therefore a novel detector, an electromagnetic calorimeter, has been developed. Ideally, such detector should be capable to estimate the temperature of the generated photons and provide their energy distribution. The thesis describes the simulations that were performed employing the Monte Carlo FLUKA code to design the calorimeter and the signal reconstruction techniques developed.

Key words: petawatt lasers, high-energy photons detector, electromagnetic calorimeter, signal unfolding, plasma physics

Contents

Introduction **1**

1 Interaction of petawatt lasers with solid targets. **2**
1.1 Basic plasma parameters 2
1.2 Propagation and absorption of laser wave in plasma 4
1.2.1 Propagation 4
1.2.2 Absorption 5
1.2.3 Hot electrons temperature scaling 8
1.3 Target ionization mechanisms 9
1.4 Laser pulse and prepulse interaction with plasma 10

2 Generation of high-energy photons in the interaction of a petawatt laser with a target **12**
2.1 Radiation from laser-plasma interaction 12
2.2 Photons-matter interaction 16
2.3 Electromagnetic cascades in matter 17

3 Overview of the most commonly used active diagnostics for the detection of high-energy radiation **20**
3.1 Electromagnetic calorimeters 20
3.1.1 Homogeneous calorimeters 21
3.1.2 Sampling calorimeters 21
3.1.3 Energy resolution 22
3.2 Scintillators 22
3.2.1 Light detectors 23

4 Simulations of high-energy photon interaction with a detector **25**
4.1 Principles of the FLUKA code 25
4.2 Simulation setup in FLUKA 26

5 Development of a novel electromagnetic calorimeter for the detection of high-energy photons **29**
5.1 Initial design and simulation setup 30
5.2 Development of the unfolding technique 32
5.2.1 Necessity of the unfolding 32
5.2.2 Gaussian elimination with pivoting 33
5.2.3 Gradient unfolding method 35

5.3 Design optimization 39
5.3.1 Material optimization 39
5.3.2 Geometry optimization 39
5.4 Discussions of the results 41
5.5 Future steps 42

Conclusion **44**

Introduction

With the advent of laser technology in the last century, it became possible to use lasers to investigate physical processes in different fields ranging from atomic to plasma and high-energy physics. One of the upcoming multi-petawatt (PW) high-intensity laser facilities is currently being built at the ELI Beamlines (Extreme Light Infrastructure) facility and aims to reach peak intensities over 10^{21} W/cm^2. The interaction of such high-power lasers with matter results in instantaneous plasma creation and subsequent emission of high-energy particles and radiation.

The high-energy photons coming from the interaction have become of a great interest in a broad range of scientific research, including inertial confinement fusion, charged particles acceleration, and laboratory astrophysics. Spectroscopy of such emission can provide with the information about the plasma particles' energy, physics of the acceleration process, etc. However, the currently used diagnostics is not suitable for the spectroscopy of copious amounts of very intensive and short high-energy photon bursts.

Therefore, a novel scintillators-based electromagnetic calorimeter capable of the photon temperature estimation has been developed in collaboration between ELIMAIA (ELI Multidisciplinary Applications of laser-Ion Acceleration) and Monte-Carlo groups from ELI Beamlines. Such a detector can be extremely useful in characterizing the high-energy photon emission from currently existing and future high intensity laser facilities. In this work the progress in the calorimeter development is summarized.

The thesis is organized as follows. The first chapter describes the theory of PW laser interaction with solid targets. The second one summarizes the physics of high-energy photons generation and principles of their interaction with matter. Chapter 3 aims to give an overview of the most common active photon diagnostics used nowadays, including principles of different electromagnetic calorimeters types and discusses their benefits and drawbacks. This is followed by Chapter 4, in which principles of the Monte Carlo code FLUKA used for the simulations of the photons-detector interaction is given.

The final chapter describes my original contribution to the development of the calorimeter. It focuses on the simulations work and on the development of an unfolding technique necessary for the signal reconstruction. It also describes the current status of the development and the steps missing for the realization of the first prototype and of the final detector.

Chapter 1

Interaction of petawatt lasers with solid targets.

Laser-plasma interaction is an exciting discipline of modern Physics that has been explored since the realization of the first laser in 1960 [1]. Over the past years laser power has reached petawatt (PW) level with over 50 PW class lasers currently operational, under construction or in the planning phase [2]. For instance, the world most intense laser system with ultra-high peak power of 10 PW will soon be available at ELI Beamlines center in Prague [3]. Such tremendous progress was possible primarily due to the invention of the chirped pulse amplification (CPA) technique that enabled obtaining ultra-short, ultra-high intensity pulses with typical duration in terms of femtoseconds, avoiding problem of destroying an amplifier medium [4].

With the development of PW lasers, previously unobtainable extreme states of matter have been achieved in laboratory. Different research fields have benefited from the usage of PW-class lasers, including particle acceleration, radiation therapy, inertial confinement fusion, and also secondary particles generation (x-rays, electrons, ions and neutrons) [2].

Focused on a target, such lasers induce a rapid ionization near the target surface and subsequent matter transformation into a dense plasma. This process happens since the electric field of the high-power laser pulse is much stronger than the Coulomb field that binds electrons and atomic nuclei. The fundamental properties of the created plasma depend on both target and laser radiation parameters. Basic plasma characteristics and principles of laser pulse propagation, interaction and absorption in plasma will be discussed in this chapter, along with the most common target ionization mechanisms.

1.1 Basic plasma parameters

Plasma is a quasineutral gas of charged and neutral particles which exhibits collective behavior [5].

The latter term means that particle motions in a plasma depend not only on local conditions but also on the state of the plasma in distant regions. This indicates, that the influence of macroscopic electromagnetic fields on the particle interactions prevails over microscopic fields occurring in binary collisions.

The concept of quasineutrality lays in the fact that the total plasma charge is much

lower than the total positive charge. Assuming that n_e and n_i denote respectively electron and ion densities and Z is the average charge of ions, the condition of quasineutrality can be expressed as

$$n_e \cong Zn_i \cong n, \tag{1.1}$$

where n is the plasma density. However, plasma appears quasineutral only locally: at spatial scales much larger than the Debye length and at time scales much larger than the reciprocal plasma frequency (will be described in the following text).

Charge fluctuations in plasma are compensated at dimensions much larger than a Debye length distance. This is the result of a phenomenon called Debye shielding, which is a fundamental property of a plasma indicating its ability to shield (screen) intrinsic electric potentials. The shielding is implemented by a slight displacement of charged plasma particles so as to reduce the effectiveness of the arisen field. Given that a "test" particle carrying non-zero charge is placed into the initially unperturbed plasma, opposite charges present in the medium start to be attracted to it, forming a cloud surrounding the test particle.

The shielding distance or thickness of such a charged cloud is called the Debye length and for the plasma electrons is defined as (neglecting the ions contribution) [5]

$$\lambda_D = \sqrt{\frac{\varepsilon_0 k_B T}{n_e e^2}}, \tag{1.2}$$

where T is the electrons temperature in K, k_B is the Bolzmann constant in J/K, n_e is electron density in m^{-3}, e is electron charge in C and ε_0 is dielectric constant (F/m). For example, for temperature $T_e = 10$ MeV and electron density of 10^{23} m^{-3} the Debye length is $\lambda_D = 0.7$ μm.

Apparently, the Debye length definition is only valid if the number of particles in the plasma is high enough to establish an effective shield. A criterion for the determination of the sufficient amount of particles is called plasma parameter and is calculated as the particles number in a Debye sphere (presuming λ_D is the sphere's radius - see Fig.1.1) [5]:

$$N_D = n_e \frac{4}{3}\pi\lambda_D^3 \simeq 1.36 \times 10^6\ T^{\frac{3}{2}} n_e^{-\frac{1}{2}}. \tag{1.3}$$

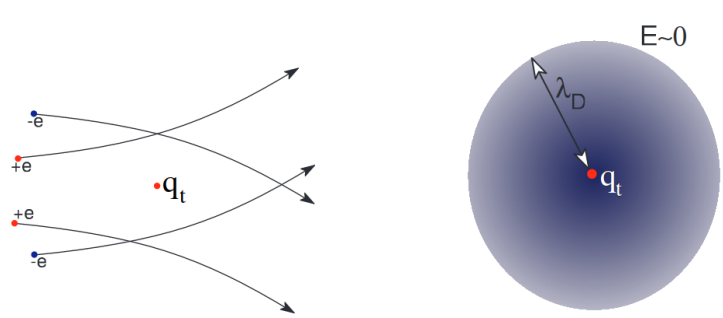

Fig. 1.1. Sketch of the particle trajectories (left) and charge distribution in the Debye sphere (right) in the vicinity of a test charge q_t. [6].

Therefore, for successful electric potentials screening, the plasma parameter ought to satisfy the following condition:

$$N_D \gg 1. \tag{1.4}$$

Due to the fact that the mass of electrons is more than 1000 times smaller than that of any ion, they are more mobile and move faster. Moving so as to surround the excess of positive charge or repulse from the excess of negative charge they mainly accomplish the Debye shielding. The eventual electric potential $\phi(r)$ in the plasma, depending on the distance r from the test particle, can be calculated according to the following equation [6]:

$$\phi(r) = \phi_0 \exp(-\frac{r}{\lambda_D}). \tag{1.5}$$

For $r \ll \lambda_D$ the potential $\phi(r)$ is identical to the Coulomb potential $\phi_0 = e/(4\pi\epsilon_0 r)$ of a test particle in vacuum, whereas for $r \gg \lambda_D$ the test charge is completely screened by its surrounding shielding cloud. Thus, the potential is exponentially damped in plasma with the strength of damping given by the Debye length. This imposes that the plasma size L have to be much greater than the Debye length:

$$L \gg \lambda_D. \tag{1.6}$$

A very important parameter in the view of the plasma collective behavior is the plasma (Langmuir) frequency. It is depicted as the oscillation frequency of an electron layer about its initial position. If some electromagnetic wave, e.g. laser pulse, interacts with plasma, electrons are slightly dislocated from their initial positions while ions are almost at rest due to their larger mass. Such charge separation generates uniform electric field and causes the restoring force. Consequently, the plasma is subjected to oscillations with frequency [5]:

$$\omega_p = \sqrt{\frac{n_e e^2}{m_e \varepsilon_0}}. \tag{1.7}$$

Collective motion in plasma prevails over binary interactions provided that the following condition is satisfied:

$$\omega_p \gg \nu_c. \tag{1.8}$$

where ν_c is the frequency of binary collisions.

1.2 Propagation and absorption of laser wave in plasma

1.2.1 Propagation

A laser pulse is an electromagnetic wave. The dispersion relation of the electromagnetic wave propagating in plasma is [7]

$$\omega^2 = \omega_p^2 + c^2 k^2 \tag{1.9}$$

where ω denotes the frequency of electromagnetic (EM) wave (laser frequency), ω_p the plasma frequency as defined by 1.7 and k is the wave vector.

Depending on the frequency ω of the laser wave, 3 cases may take place:

- $\omega > \omega_p$, then k is real and the wave propagates through the plasma. It happens since the electrons are not able to follow the field oscillations because of their own inertia, thus the plasma acts as a transparent media for the laser wave. Such a plasma is called underdense plasma.

- $\omega < \omega_p$, then k is imaginary and the laser wave is reflected from the plasma. However, an exponentially decaying field is transmitted across the barrier and propagates into the plasma until a finite depth - the collisionless skin depth $l_s = c/\omega_p$. In this situation the plasma is called overdense.

- $\omega \simeq \omega_p$, then $k \simeq 0$, the wave is reflected, as the electrons oscillating in the laser field impede its propagation. The electron density corresponding to the laser wave reflection is called *critical density* and is calculated as [8]

$$n_{cr} = \frac{\varepsilon_0 m_e}{e^2}\omega^2 = 1.1 \times 10^{15} m^{-3} \left(\frac{\lambda}{1\mu m}\right)^{-2} \tag{1.10}$$

  So, the critical density distinguishes between the underdense and the overdense plasma regimes.

Whether the wave is reflected or it propagates through the plasma, it interacts with the electrons and ions of this medium and affects their motion. The motion of charged particles in the electromagnetic field of a laser is governed by the Lorentz force [5]:

$$\vec{F_l} = q\left(\vec{E} + \vec{v} \times \vec{B}\right), \tag{1.11}$$

where q is the charge of a particle, $\vec{E}$ is the electric and $\vec{B}$ is the magnetic field of the laser.

1.2.2 Absorption

Laser radiation energy is transferred to the plasma via electrons, which interact with the laser wave first due to their high inertia, and then is distributed to heavier ions.

Absorption of the laser light by the plasma electrons can proceed either by collisions with nucleus or through collisionless mechanisms. Inverse Bremsstrahlung mechanism is an example of collisional absorption: an electron gains its kinetic energy from an oscillating laser wave and is subsequently thermalized by collisions with atomic nuclei [9]. The collisional frequency ν_{ei} between ions and electrons is defined as [10]:

$$\nu_{ei} = \frac{3Z^2 e^4 n_i \ln \Lambda}{8\pi\epsilon^2 m_e^2 v_e^3}, \tag{1.12}$$

where $\ln \Lambda$ is the Coulomb logarithm and Z is the ion charge number.

Since the frequency is in inverse ratio to the electron velocity v_e, an increasing energy of the electrons implies its rapid reduction. The kinetic energy of the electrons depends

directly on the incident laser intensity (irradiance) I_L [11], which can be approximated as:

$$I_L \lambda_L = a_0^2 \times 1.37 \times 10^{18} \text{ W}\mu\text{m}^2\text{cm}^{-2}, \tag{1.13}$$

where a_0 is a dimensionless amplitude that governs electrons motion [12]:

$$a_0 = \frac{eA_0}{m_e \omega c}, \tag{1.14}$$

where λ_L is the laser wavelength, A_0 is the vector potential, e and m_e are the electron charge and mass and w is angular frequency.

In the case of $a_0 \gg 1$ and hence $I_L \lambda_L > 10^{18}$ Wμm^{2}cm^{-2}, a significant number of plasma electrons is accelerated up to relativistic velocities during a few cycles of the laser electric field, and the plasma becomes essentially collisionless.

With the use of PW-peak-power lasers intensities greater than 10^{21} Wcm^{-2} can be achieved. This is beyond the relativistic threshold for velocities of the electrons oscillating in the laser field [13], [14]. Therefore, collisional absorption of PW laser becomes negligible in comparison to other absorption mechanisms that start to prevail. These mechanisms are called collisionless and are briefly described in the following text (in more detail see [15]).

- **Resonance absorption**

This mechanism lies in resonant excitation of an electron plasma wave which then propagates into the overdense plasma.

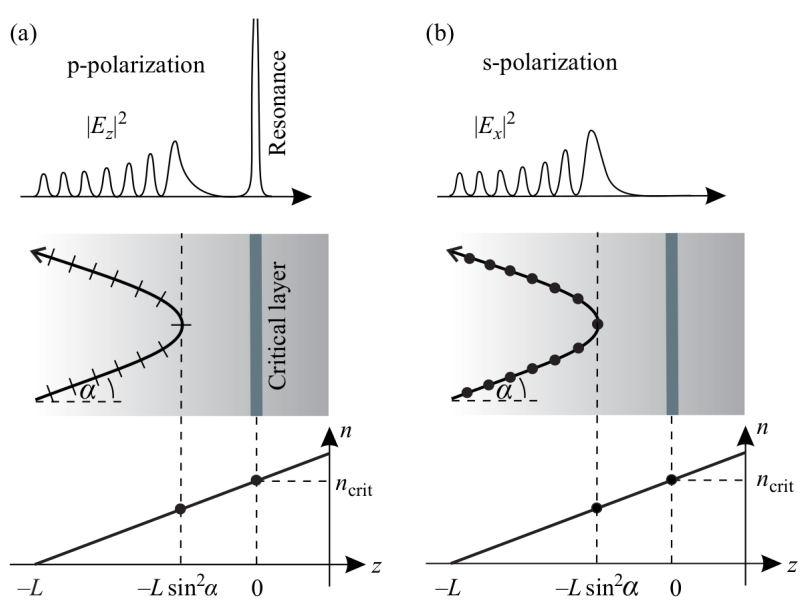

Fig. 1.2. Sketch of the resonance absorption mechanism for a) p-polarized laser and b) s-polarized laser wave [16].

Pre-expansion of the plasma caused by a laser prepulse (see section 1.4) results in the formation of a density gradient, and the resonance occurs in the region where the plasma

frequency ω_p equals the laser frequency ω (follows from Eq. (1.7)). This mechanism is valid only for p-polarized waves, since the electric field $\vec{E}$ of such waves lies in the direction of the density gradient. Therefore, it can resonantly excite electron plasma (Langmuir) wave in the critical layer by separating positive and negative charges. On the contrary, in the case of s-polarized wave no resonance, and hence energy transfer, is achievable. Illustration of the resonant absorption for both polarization cases is presented in Fig.1.2.

- **Brunel heating**

This type of absorption occurs in high intensity laser-plasma interaction when steep density gradients and obliquely incident p-polarized laser wave are considered. As this mechanism was firstly described by Brunel in 1987 [17], it is also known as Brunel heating.

If the electron oscillation amplitude exceeds density gradient scale length, then the electrons of the plasma-vacuum boundary are pulled out from the plasma under the influence of the laser pulse's electric field. When the field changes its direction during later phase, accelerated electrons are injected back into the plasma. Given that the laser field is attenuated in the overdense plasma, electrons can propagate further uninfluenced, and a part of the laser energy they carry is completely scattered in the plasma. Stages of this process are depicted on Fig.1.3.

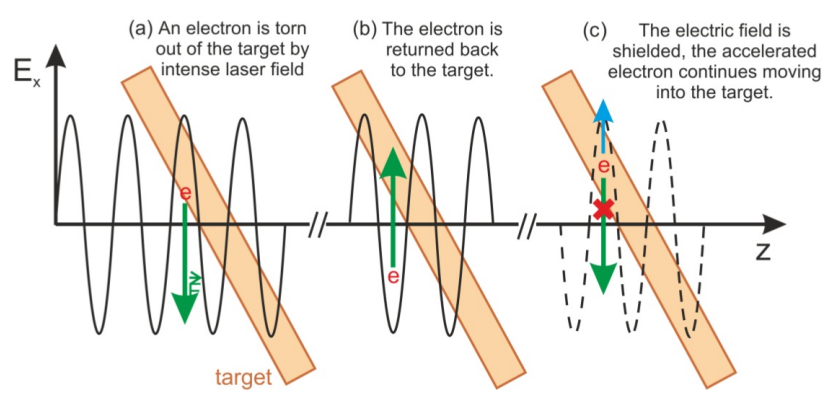

Fig. 1.3. Stages of Brunel heating process [18].

- **j×B heating**

Similarly to the Brunel heating, $\vec{\mathrm{j}} \times \vec{\mathrm{B}}$ mechanism also requires a very steep density gradient of plasma. The difference is that in this process electron motion is treated as relativistic and hence the magnetic component of the Lorenz force (Eq. 1.11) becomes significant, whilst in the vacuum heating electrons were driven only by the electric field. Thus, electrons are extracted into vacuum twice during the laser cycle by combination of the electric and the magnetic fields, whereas in Brunel heating only once.

The advantage of this mechanism is that due to the magnetic component it can be efficient even for perpendicular incidence of the laser pulse and for s-polarized wave.

1.2.3 Hot electrons temperature scaling

Even if the laser is reflected back, a significant fraction of its energy may be transferred to the electrons of the target by one of the collisionless mechanisms described above. Usually, the energy is distributed to a small fraction of plasma electrons, which are referred to as "hot electrons". Such particles can be heated up to extremely high temperature (hundreds of keV− tens of MeV), while that of the rest of the plasma electrons stay at relatively lower level. Therefore, plasma electron population acquires bi-Maxwellian energy spectrum with two characteristic temperatures named T_h and T_e [19]. Maxwell-Bolzmann (MB) energy distribution is defined as:

$$f(E) = 2\sqrt{\frac{E}{\pi}}\left(\frac{1}{kT}\right)^{3/2} e^{-E/kT}, \tag{1.15}$$

where E is the electron energy and k is the Boltzmann constant. A typical bi-Maxwellian distribution for plasma electrons is shown in Fig. 1.4.

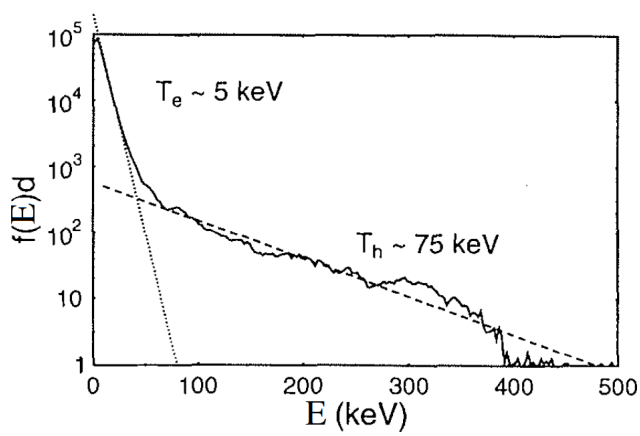

Fig. 1.4. Typical example of bi-Maxwellian electron distribution resulting from collisionless heating by laser [19].

In recent years, scaling laws for determination of the hot electron temperature and hence energy spectrum were introduced (ponderomotive scaling [31], Beg's scaling [21], etc.). The temperature appeared to be proportional to the laser intensity multiplied by the laser wavelength: $T_h \sim (I\lambda)^\alpha$, where coefficient α can be different depending on the scaling law. For laser intensities up to $I\lambda^2 = 8 \times 10^{20}$ W cm^{-2}, the empirically derived Beg's scaling with $\alpha = 0.3$ is the mostly used nowadays, as different experimental data correspond with the law [22].

Recent simulation results indicate that right after the laser-plasma interaction the hot electron temperature satisfies [23]:

$$T_h(MeV) = 1.01\left(\frac{I\lambda^2}{10^{18}\mathrm{Wcm}^{-2}\mu\mathrm{m}^2}\right)^{1/3}. \tag{1.16}$$

which also agrees with the Beg's scaling.

However, for higher laser intensities beyond $10^{19} - 10^{21}$ W cm^{-2}, there are still little experimental data available to clarify the T_h scaling law. Nevertheless, as it

was demonstrated recently, the scaling is also strongly dependent on the absorption mechanisms and the laser incidence, which can lead to the α coefficient varying from ~ 0.3 to ~ 0.6 [23, 24, 25].

Hot electron temperature predictions can be further used, for instance, to estimate the temperature of photons emitted by these electrons (Bremsstrahlung – see Chap.2) for diagnostics' development.

For ultrahigh laser intensities of 10^{22} and 10^{23} W cm^{-2}, which might be achieved by ELI Beamlines PW-class lasers, the hot electrons temperature scaling is yet obscure due to the absence of experimental data. However, using Eq. (1.16) we can estimate that it might be in the range $(22; 47)$ MeV, where the first number is calculated for the intensity of 10^{22} W cm^{-2} and the second for the intensity of 10^{23} W cm^{-2}.

1.3 Target ionization mechanisms

In real experiments, before the laser-plasma interaction can occur, the target material (solid, gaseos or liquid) should be turned into plasma, i.e. ionized by the incident laser pulse. For this reason, a brief description of target ionization mechanisms will be introduced in this chapter.

The intensity at which the electric field of the laser equals the binding strength of the electron to the nucleus is called atomic intensity and is approximated as [19]:

$$I_a \simeq 3.51 \times 10^{16} \text{ W cm}^{-2} \tag{1.17}$$

Lasers (including PW laser systems) with intensities exceeding the atomic one will guarantee the ionization of the target medium.

- **Multiphoton ionization**

If the photon energy is higher than the electron binding energy, then the electron can be ejected from the atom upon absorption of single or multiple photons. However, since lasers mostly operate in the visible or infrared spectral range (where the single photon energy is insufficient for ionization), multiphoton ionization generally takes place. In this case electron absorbs several lower frequency photons on a short timescale and by combining their energies reaches the ionization threshold.

- **Tunnel ionization and Coulomb barrier suppression**

With the increasing laser intensity, the electric field becomes strong enough to significantly distort the atomic potential. Once the distortion results in a sufficient suppression of the Coulomb barrier, the electron can tunnel through it and reach the continuum state. For larger distortions the Coulomb barrier can be lowered beneath the binding energy of the electron and eventually the particle can just cross it.

To separate the multiphoton and the tunneling ionization, the Keldysh parameter γ_K was introduced [26]:

$$\gamma_K = \sqrt{\frac{V_{ion}}{2U_p}}, \tag{1.18}$$

where V_{ion} is the ionization potential of the electronic state and $U_p = e^2|\mathbf{E}|^2/(4m_e w^2)$ is the laser ponderomotive potential, which is the average energy of the electron oscillating in the field of an electromagnetic wave with frequency w and electric field amplitude E.

The Keldysh parameter indicates which mechanism would be dominant in the given experimental conditions. The two processes are efficient in different regimes of the frequency spectrum: tunneling becomes significant for high intensities and high frequencies, i.e., for $\gamma_K \ll 1$, while for $\gamma_K \gg 1$ multiphoton ionization prevails.

- **Collisional ionization**

In dense plasmas which usually emerge from solid targets, collisional ionization mechanism becomes important. This mechanism is associated with inelastic collisions of free electrons with ions. Once a sufficient number of free electrons is produced by means of field ionization, collisional processes come into play. Comprehensive theory on this type of absorption can be found in [27].

1.4 Laser pulse and prepulse interaction with plasma

At present, a femtosecond laser pulse is typically obtained with the CPA technique. However, a CPA laser system generates not only a clean ultrashort main pulse, but also a relatively low-energy nanosecond prepulse (or pedestal) which precedes the main one. The main sources of prepulse in any laser system are [28]: nanosecond amplified spontaneous emission (ASE) from the amplification chain; femtosecond prepulses from the imperfect isolation of the main pulse; and picosecond pedestal due to imperfect recompression of the chirped pulse.

The presence of the prepulse plays an important role especially in interaction with solid targets, because the pedestal can greatly affect the density conditions of the target before its interaction with the main pulse. In fact, the prepulses incident on a target would vaporize it and turn it into plasma, because the ASE level in CPA lasers is above the ionization threshold of many types of targets. The main ultrashort pulse will subsequently interact with a lower-density plasma instead of a solid target. This can make many types of experiments and possible applications challenging and problematic (e.g. usage of ultra-thin (μm,sub μm) targets [29], targets with nanostructures [30], decrease in the maximum achievable ion energy in the TNSA (Target Normal Sheath Acceleration [31]) regime [32]).

For PW laser pulses, the pedestal intensity has to reach up to 10^{-12} times intensity of the main pulse (depending on the the material properties) in order to prevent the expansion of the preplasma and to avoid undesirable effects [33]. However, standard CPA laser systems show contrast ratios around 10^{-6}–10^{-8} which are not sufficient for these purposes.

Nevertheless, different methods of improving the laser contrast have been developed. For example, using an optical device called a plasma mirror (PM): it is a plate of a dielectric material covered with an anti-reflected layer, where the laser beam is focused. When the low-intensity prepulse is incident on this layer, it will be transmitted without damaging the PM surface. With the increase of the laser pulse intensity, the critical plasma can be created on the surface of PM, which reflects the most part of the main pulse like a metallic mirror. An optical system based on two subsequent plasma mirrors

is called Double Plasma Mirror (DPM) [34]. The usage of such system results in the final contrast of at least 10^{-10}.

Furthermore, pulse cleaning techniques are employed to decrease the prepulse intensity below the ionization threshold by increasing the seeding energy of the amplifiers [35]. To generate a suitable seed pulse, the double CPA technique [36] is used. Other methods include, inter alia, the uOPA technique [33] and the usage of saturable absorbers [37].

Chapter 2

Generation of high-energy photons in the interaction of a petawatt laser with a target

The interaction of a high-power pulsed laser with a target is normally accompanied by the emission of high-energy charged particles, neutral particles, and photons. The energetic photons are characterized by very short wavelengths and fall within the X-rays and gamma-rays (γ-rays) region of the electromagnetic (EM) spectrum[1].

The generation of such radiation is not only an active field in fundamental research [39], but is also a useful tool in different applications, such as radiography of dense objects [40], radiation chemistry [41] and cancer radiotherapy [42]. In particle physics, detection of emitted gamma and X-rays from the interaction can provide particular information (energy, space distribution) about the particles that produced them [*couldn't find references*].

Various processes causing the photon emission can prevail depending primarily on the laser intensity and the target type (which affects the characteristics of the produced plasma). Processes significant for PW class lasers of intensities $10^{21} - 10^{23}$ W cm^{-2} will be briefly described in this chapter, along with the photon-matter interaction mechanisms.

2.1 Radiation from laser-plasma interaction

- **Bremsstrahlung radiation**

Bremsstrahlung is the dominant radiation process in solids under intense laser irradiation and currently is of a great research interest [43, 44, 45].

Such radiation results from deceleration of a charged particle in the field of another charged particle due to Coulomb interactions, typically an electron in the field of atomic nuclei of the target material. The reason why only decelerated (or accelerated) charged particles are capable of producing this type of radiation is, that during non-constant motion, the non-static electric and magnetic fields of a charged particle can not adjust

[1] There is no explicit boundary between X-rays and γ-rays, although photons carrying kinetic energies over 100 keV are usually called gamma photons [38].

themselves so that no energy is radiated away. Therefore, decelerating in the field of a nucleus, charged particles lose part of their kinetic energy in the form of bremsstrahlung photons. A scheme of this process is sketched in Fig. 2.1.

The power P emitted in the form of the bremsstrahlung radiation is in inverse proportion to the charged particle's mass, therefore only electrons and positrons can efficiently radiate, while the contribution of heavy charged particles (protons, deuterons, alpha particles and heavier ions) is negligible. The power is also proportional to the atomic number Z of the target material, thereby more photons are generated in high-Z absorbers [46]:

$$P = \frac{\mathrm{d}E}{\mathrm{d}t} \sim \frac{Z^2}{m^2} \tag{2.1}$$

The energy of the emitted bremsstrahlung photons ranges from zero up to the maximum kinetic energy of the incident electron, resulting in a broad and continuous spectrum (see Fig. 2.2). As can be seen from the figure, the emission of low-energy photons usually dominates, while towards the higher energies the spectrum drops to zero.

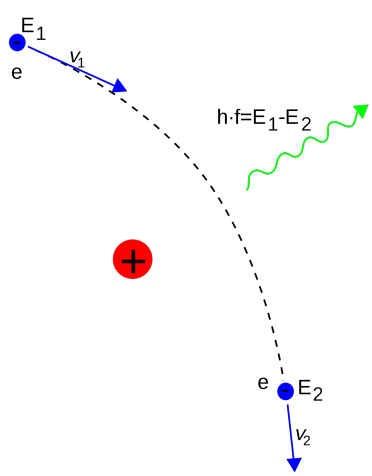

Fig. 2.1. Bremsstrahlung X-rays generated due to electron declaration in the field of a nucleus [47].

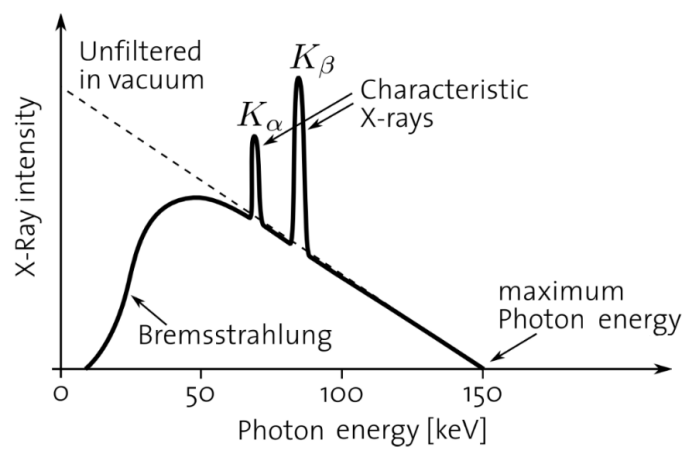

Fig. 2.2. Continuous bremsstrahlung spectrum with characteristic K_α and K_β lines [47].

- **Characteristic radiation**

In addition to the bremsstrahlung radiation, the characteristic X-rays are also produced during the electron-matter interaction. They result from the transitions of the bound electrons in atoms triggered by the vacancies in inner electronic shells of the atom.

Vacancies in atomic shells appear due to the orbital electrons disruption from their normal configuration induced by some excitation process (excitation by radioactive decay or external radiation). An atom with a vacancy remains in an excited state for a short period of time and subsequently returns to its ground state through one or several electron transitions. During such transitions, the electron from a higher-level atomic shell fills the orbital vacancy. The energy difference between the initial and

the final shell is subsequently emitted either in the form of characteristic radiation or radiation-less, being transferred to an orbital electron that is afterwards ejected from the atom as an Auger or Coster–Kronig electron [48].

The radiation in this process is referred to as characteristic, since the emitted photons have certain discrete energies $\hbar\omega$ and wavelengths λ that are characteristic of the particular atom from which the photons are originated. The set of the characteristic photons emitted from a given atom is called the line spectrum of the atom and can be employed for energy calibration of radiation detectors.

The most significant characteristic lines generally present in the spectrum are K_α and K_β X-rays (see Fig. 2.2): in Siegbhan notation [49], K_α ray is emitted by an electron transition from the L-shell of the atom to the K-shell, and K_β ray by the transition from the M-shell to the K-shell.

However, for laser intensities exceeding 10^{20} W cm^{-2}, K_α and K_β emission are typically weak and of low frequencies when compared with bremsstrahlung radiation [50].

- **Compton and Thomson scattering**

Part of the photons coming from the laser-plasma interaction are emitted due to the Compton scattering process. It is an incoherent scattering of a photon on an essentially free (loosely bound) orbital electron. The incident photon energy in this case is much greater than the binding energy of the orbital electron. In this process, an incoming photon strikes the electron (assumed to be initially at rest) and transfers to it some of its kinetic energy E_K: the electron is consequently ejected from the atom as a recoil (Compton) electron. Simultaneously, a scattered photon with energy $\hbar\nu' = \hbar\omega - E_K$ is produced, deflected through a scattering angle θ with respect to the direction of the original photon, as shown schematically in Fig. 2.3.

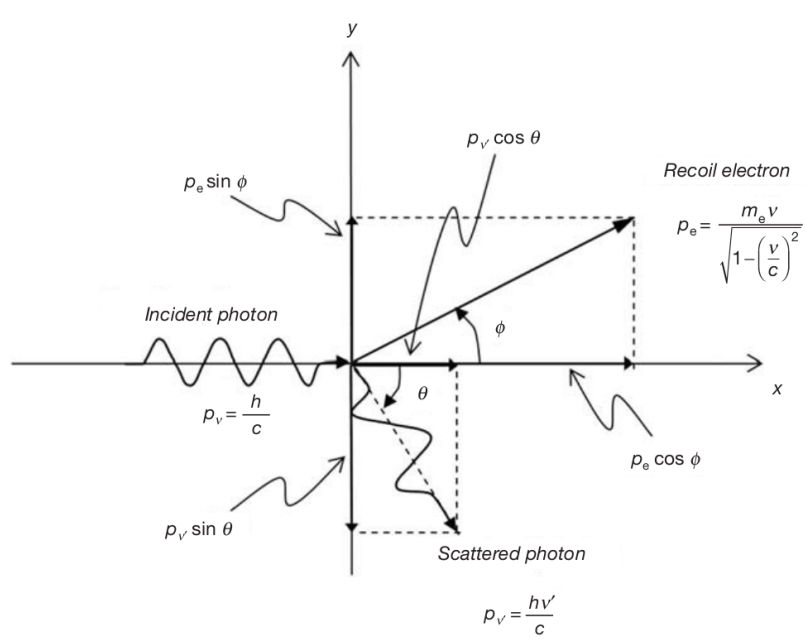

Fig. 2.3. Schematic diagram of the linear Compton scattering. [51].

The low-energy (nonrelativistic) limit of Compton scattering which does not imply change in the particle kinetic energy and photon frequency is called the Thomson scattering.

Collisions between an electron and the laser pulse of high intensity results in the emission of gamma photons in the nonlinear or multi-photon Compton scattering regime. The latter one is characterized by independent multiple scattering of the electron and is physically distinct from nonlinear Compton scattering in which several photons are absorbed at a single point, but only a single high-energy photon is emitted. For theoretical aspects see [52, 53].

As it was demonstrated recently, contributions from nonlinear Compton scattering appear when laser intensities are larger than 10^{21} W cm^{-2}, as quantum effects in the framework of the QED (Quantum Electrodynamics) theory become considerable. A threshold intensity under which nonlinear Compton scattering becomes even dominant over bremsstrahlung radiation is an open issue of current research: according to [45], it is 10^{24} W cm^{-2}, but simulations performed in [54, 55] predict the threshold to be at 10^{22} W cm^{-2}.

The angular distribution of scattered photons is predicted by Klein-Nishina formula for the differential scattering cross-section [56] and is presented in Fig 2.4. A strong tendency for forward scattering for high-energetic photons is noticeable from the figure. Such distribution was further confirmed by multiple simulations ([57] and references therein).

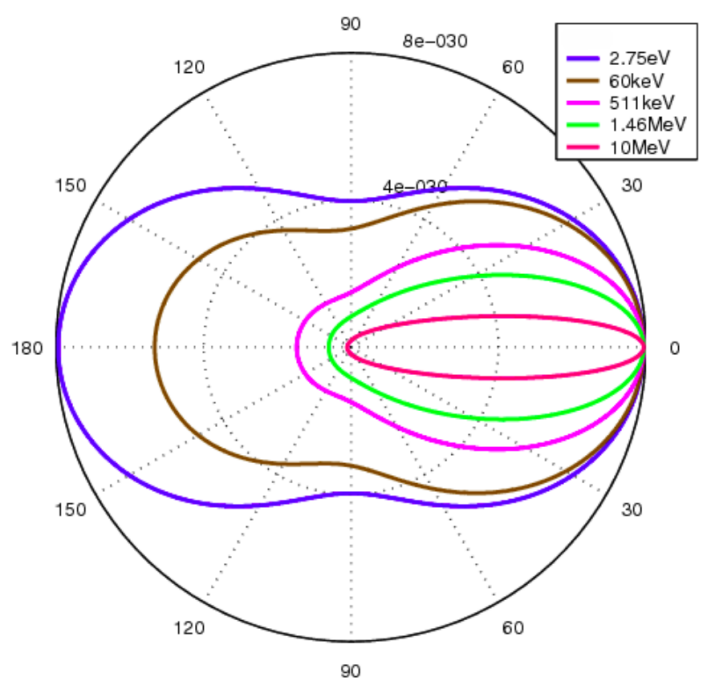

Fig. 2.4. Klein–Nishina distribution of scattering-angle cross sections over a range of commonly encountered energies. [58].

2.2 Photons-matter interaction

Penetrating through the matter, photons may experience a large number of interactions with the material atoms; the probability of the cross-section for each interaction mechanism depends on the energy of the impinging photon $\hbar\omega$ and the atomic number Z of the absorbing material. These interactions involve either the nuclei of the absorbing material (*photodisintegration, pair production*) or its orbital electrons, that, in turn, can be divided into tightly bound electrons (*photoelectric effect, Rayleigh scattering*) and essentially free orbital electrons (*Thomson scattering, Compton scattering, pair production*). After the interaction with an atom the photon may completely disappear (its energy is fully absorbed and transferred to light charged particles) or it may be scattered either coherently (with no change in the photon energy) or incoherently (with the resulting scattered photon having a lower energy than the incident one).

Although different interaction mechanisms are possible, only three of them are crucial in radiation measurements (especially of X-rays and γ-rays): photoelectric absorption, linear Compton scattering, and pair production.

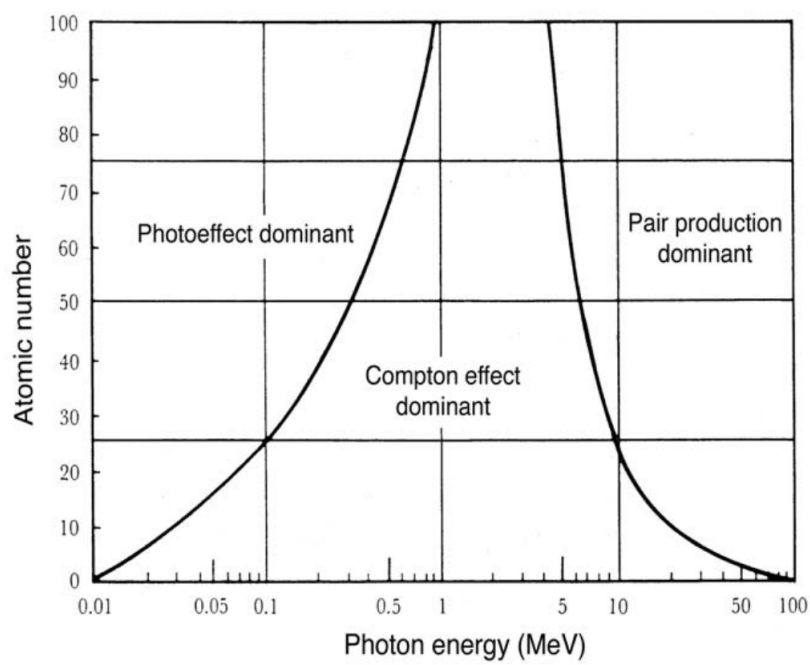

Fig. 2.5. Regions of relative predominance of the three main mechanisms of photon interaction with matter. [51].

The photoelectric absorption is the dominant process for the radiation of low energy (up to several hundreds keV). Linear Compton scattering is most probable for the photons in the "medium" energy range (from several hundreds keV to several MeV). The cross-section depends on the number of electrons in the absorber medium available for the interaction and hence increases linearly with the atomic number Z. On the other hand, the probability of this process decreases with increasing energy of photons. For high-energy photons (above 5-10 MeV) electron-positron pair production in the nuclear Coulomb field becomes the most probable photon-matter interaction mechanism. Ma-

terials with higher atomic numbers more readily convert photons into electron-positron pairs in comparison to low atomic number ones. Additionally, unlike the Compton and photoeffect cross section, the pair production cross section increases with increased photon energy. The relative predominance of the three processes is schematically illustrated in Fig. 2.5 The lines on the scheme correspond to regions where bordering effects are equally probable.

2.3 Electromagnetic cascades in matter

Interaction of high-energetic photons or electrons with matter may entail a process called an electromagnetic cascade. During this process, a high energy primary interacts with the medium to produce multiple less energetic secondaries, which interact producing more secondaries, continuing the process until there is enough energy. High-energy photons mainly undergo pair production and Compton scattering, while energetic electrons and positrons undergo bremsstrahlung interaction, leading to production of more photons. Because of such a spreading and multiplicative nature, this process is often referred to as the electromagnetic shower. A sketch of the process is presented in Fig. 2.6. The electromagnetic shower is always initiated by an electron or a photon and the generated particles include only electrons, positrons and photons. The extent of the process is dictated by the magnitude of the incident-particle's energy.

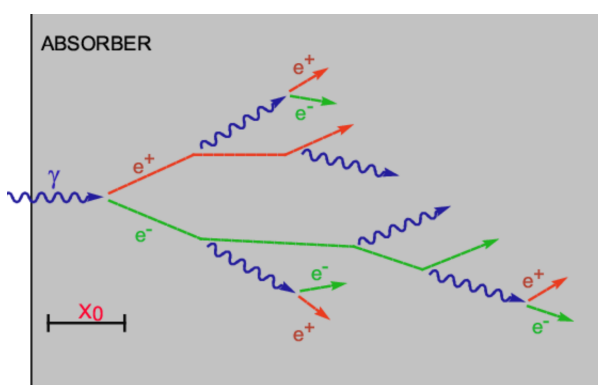

Fig. 2.6. A schematic description of the electromagnetic shower development principle. [59].

Typically, shower's expansion exhibits cone-like shape, with the vertex represented by the initially incident particle. As the original particle's energy increases, the penetration depth grows as well , while the opening angle of the cone rather decreases, given that particles of high energy are deflected less in matter.

The energy below which particles within the cascade no longer engenders further particles is termed the critical energy ϵ_c. After such threshold, photons transfer the remaining energy to the medium via the photoelectric process, while electrons dissipate it through collisions with other particles. In this manner, the incident energy is absorbed by the medium. Special detectors constructed to measure the energy deposited in their volume from such an energy degradation are called electromagnetic calorimeters (see Chapter 3).

The characteristic quantities described in the following text are essential for the understanding of the electromagnetic cascades. In the shower process, the energy is propagated both laterally and longitudinally within the material. Longitudinal development is governed by the so called radiation length X_0, while lateral shower width scales with Molière radius R_M:

- *the radiation length* represents the mean path length required to reduce the energy of high-energy particles by the factor 1/e as they pass through matter and is denoted by X_0 (in units of cm) or by X_{g0} (in units of g/cm^2).

  This quantity is a material constant, depending on the atomic number Z, mass number A, and density of absorber ρ, commonly approximated by [60]:

$$X_0 \approx \frac{A}{\rho Z^2} \quad \text{[cm]}. \tag{2.2}$$

- As it was mentioned above, *the critical energy* ϵ_c is an approximation of the energy at which electron's radiation losses via bremsstrahlung become equal to collisional losses via excitation and ionization. Below this value of energy, charged particles no longer contribute to the development of the electromagnetic cascade. One of the approximated formulas for the critical energy is given by [61]:

$$\epsilon_c = B\left(\frac{ZX_0g}{A}\right)^h \quad \text{[MeV]}, \tag{2.3}$$

  where A is the mass number of the absorber, X_0g is the radiation length in g/cm^2 and $B = 2.66$ and $h = 1.11$ are constants.

- *The Molière radius* characterizes the material giving the scale of the transverse dimension of the fully contained electromagnetic showers initiated by an incident high energy electron or photon.

  The Molière radius is in fact a radius of a cylinder around the original track of the particle, comprising nearly 90% of the energy deposited in electromagnetic shower. It is defined as [62]:

$$R_M = \left(\frac{E_s}{\epsilon_c}\right) X_0 \quad \text{[cm]}, \tag{2.4}$$

  where $E_s = m_e c^2\sqrt{4\pi/\alpha} \approx 21.2$ MeV is the scale energy calculated from the universal constants including the fine structure constant α, ϵ_c is the critical energy and X_0 is the radiation length.

Quantitative values of described quantities for some absorbers used for calorimeters are presented in Table 2.1.

Material	X_0 [cm]	R_M [cm]	E_c [MeV]
Al	8.89	4.68	40.28
BGO	1.12	2.33	10.20
Pb	0.56	1.60	7.42
U	0.32	1.00	6.77
Water	36.08	10.91	70.10

Table 2.1: Values of the radiation length for different absorber materials. [**?**].

Chapter 3

Overview of the most commonly used active diagnostics for the detection of high-energy radiation

The detection of high-energy radiation is a significant challenge in laser-plasma experiments. Over the years, multiple detectors have been developed and employed, including thermo-luminescent dosimeters (TLDs) [63], detectors employing photo-nuclear reactions [64] and image plate (IP) detectors (filter stack spectrometers [65], spectrometer based on Compton scattering [66]). However, TLDs can not provide any spectral information and the use of the photo-nuclear reactions or IPs requires complex and time-demanding post-processing, making high-repetition regime impossible.

The interaction of PW-class lasers with matter causes the generation of very intense (over 20 MeV) and short (fs) photon bursts, putting new requirements on the radiation diagnostics, among which is ability to work in high-repetition regime, providing an immediate feedback on the experiment (so called "active" diagnostics). Such devices as electromagnetic calorimeters fall within the active detectors and are suitable for the spectroscopy of short and energetic radiation. This chapter includes an overview of the electromagnetic calorimeters and gives a brief description of scintillators as the most common material used to construct such devices.

3.1 Electromagnetic calorimeters

Calorimeters are detectors designed to measure the energy deposited by an incident particle. Such devices can be divided into 2 categories according to the type of the particles of the interest: electromagnetic (EM) calorimeters, which are used to measure electrons and photons through their electromagnetic interactions (e.g. bremsstrahlung, pair production), and hadronic calorimeters for the detection of hadrons through their strong and electromagnetic interactions. In this work the focus is laid on the EM calorimeters (for information on hadronic calorimeters see section 33.9.2. in [67]).

The energy deposition in the EM calorimeters occurs through the development of electromagnetic cascades (as already discussed in the section 2.3 "Electromagnetic cascades in matter"). Therefore, the detector length increases logarithmically with the energy of incident particles, making calorimeters space and hence cost effective for

high-energy measurements. Typically, an EM calorimeter tends to be 15-30 X_0 deep. Additionally, the calorimeter energy resolution improves with the energy as $1/\sqrt{E}$ (see section 3.1.3) , where E is the energy of the incident particle, making calorimeters appropriate for the high-energy physics experiments. Furthermore, they can be used to determine the shower position and its direction and also to measure the arrival time of the particles.

According to the construction technique, calorimeters can be classified into homogeneous and sampling calorimeters.

3.1.1 Homogeneous calorimeters

The entire volume of a homogeneous calorimeter is sensitive and contributes to the signal. This results in a better energy resolution of such devices, as the primary energy is fully deposited in the active part, in contrast to the sampling calorimeters. However, they are not able to accomplish position measurements, since being less easily longitudinally and laterally segmented. Additionally, their cost can be quite high. Homogeneous calorimeters may be made of inorganic heavy scintillators (such as BGO, CsI, NaI, PWO), semiconductors, Cherenkov radiators, or ionizing noble liquids [68]. Schematic view of a homogeneous calorimeter is sketched in Fig. 3.1 on the left.

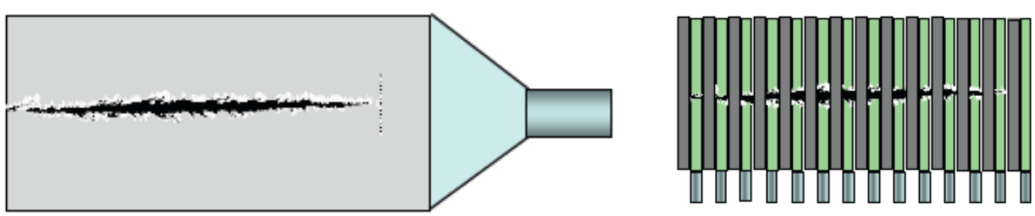

Fig. 3.1. Schematic of a homogeneous (left) and a sampling calorimeter (right) with a developing electromagnetic shower inside [69].

3.1.2 Sampling calorimeters

A sampling calorimeter consists of alternating layers of passive medium (metallic absorber) and active material which generates the signal. The active medium may be a scintillator (both organic and inorganic), an ionizing noble liquid, a gas chamber, or a semiconductor. The absorber is typically represented by a material of high density and high atomic number (lead, iron, copper). Such structure implies that the energy resolution is worse than that of homogeneous calorimeters due to fluctuations produced by the absorber layers interleaved with the active layers. On the other hand, sampling calorimeters can be more compact (and hence cheaper) if a high density absorber is chosen. Additionally, they can provide with spatial resolution, since they are easily segmented. The positional resolution depends on the Moilere radius (Eq. 2.4). Schematic of a sampling calorimeter is shown in Fig. 3.1 on the right.

3.1.3 Energy resolution

The energy resolution $\sigma(E)/\sqrt{E}$ of a calorimeter can be parametrized as $a/\sqrt{E} \oplus b \oplus c/E$, where $\oplus$ represents addition in quadrature and E is in GeV [67]. The stochastic term a is due to the fluctuations related to the physical development of the shower. For a homogeneous calorimeter the term a is usually at a few percent level, while for sampling calorimeters it is in the range 5-20% [68]. Term b is called a systematic (or constant) term and is affected by the detector non-uniformity, calibration uncertainty and radiation damage of the active medium. This term can be reduced below one percent by developing radiation-hard active media [70] and by regular calibration and monitoring [71]. The term c is due to the electronic noise of the readout chain. Some examples of the energy resolution for different calorimeters are presented in Table 3.1.

Material (experiment)	Depth	Energy resolution
CsI (KTeV)	$27X_0$	$2\%/\sqrt{E} \oplus 0.45\%$
PWO (CMS)	$25X_0$	$3\%/\sqrt{E} \oplus 0.5\% \oplus 0.2/E$
Scintillator/Pb (CDF)	$18X_0$	$13.5\%/\sqrt{E}$
Scintillator fiber/Pb (KLOE)	$15X_0$	$5.7\%/\sqrt{E} \oplus 0.6\%$

Table 3.1: Energy resolution of typical electromagnetic calorimeters: the first two are homogeneous, the last two are sampling. The latter ones have worse resolution, but their size is smaller in comparison to homogeneous devices [67].

.

3.2 Scintillators

A scintillator is a luminescent material that emits visible light when it absorbs high-energy radiation due to the de-excitation of the atoms ionized by the incident photons. Scintillator crystals are resistant to electromagnetic pulses (EMP) accompanying each high-intensity laser-plasma interaction, active (i.e. provide with a signal in a real-time regime), and in a calorimeter setup they can provide spectral information.

To be successfully employed in photon detection, a scintillation material should possess certain properties, such as i) easily detectable emitted light with a high scintillation efficiency, ii) light yield proportional to the deposited energy (linear conversion), iii) transparency to the wavelength of its own emission, iv) short decay time of the induced luminescence (enabling fast signals generation), v) firm enough to be manufactured in sufficiently large sizes and to remain in good optical quality and vi) index of refraction suitable for scintillator coupling to the light detector.

The scintillation material may be organic or inorganic. The latter is more commonly used for the high-energy photon detection due to the high atomic number and density. Small amounts of impurities (called activators) are added to most inorganic scintillators to enhance the emission of visible photons, as atomic de-excitations in this case can be channeled through these impurities and lead to the emission of detectable visible light. Good examples of such crystals are commonly used sodium iodide NaI(Tl) and cesium iodide CSI(Tl) scintillator materials which are doped with thallium. However, there are

some inorganic materials that do not require doping: bismuth germanate $Bi_4Ge_3O_{12}$ and lead tungstate $PbWO_4$ (commonly referred to as BGO and PWO, respectively). The inorganics are usually characterized with the best light output and linearity, but mostly are relatively slow in their response time.

Organic scintillators are aromatic hydrocarbon compounds containing a benzenic cycle (e.g. anthracene, plastics). During the de-excitation, organic scintillators emit bands of ultraviolet (UV) light which can be absorbed by most organic materials in a few mm length. Hence, to extract the produced light, another fluorescent material called a wavelength shifter (WS) is used, that contributes to the conversion of UV into visible light. WSs can also be used for transporting the scintillation light to photosensetive devices if light has to be collected at a location distant from the scintillator. Organic scintillators are generally faster than inorganic ones, but not linear and have low density and low atomic number and, therefore, yield less light and have relatively low absorption for gamma and X-rays [48].

3.2.1 Light detectors

The light pulse from the scintillator is subsequently converted into electrical signal by a light detector. The most frequently used detectors are the photomultiplier tube (PMT) and the charge coupled device (CCD).

Photomultiplier tube

The PMT is usually coupled to the scintillation crystal via light guides. A schematic view of the scintillator-PMT coupling is shown in Fig 3.2.

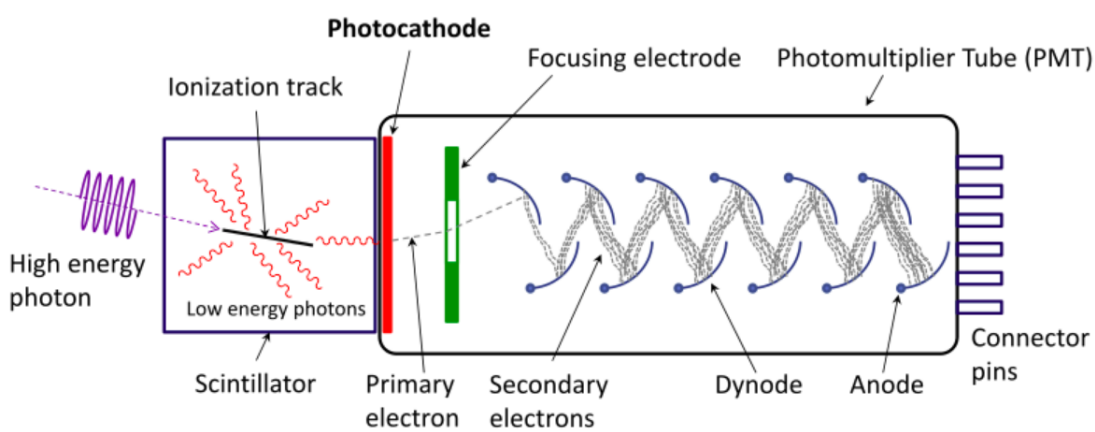

Fig. 3.2. Schematic of high energy photon hitting a scintillator material and inducing the release of low-energy photons which are then converted into photoelectrons subjected to further multiplication in photomultiplier tube [72].

As can be seen from the figure, the first element of the PMT facing the incident light is a photocathode. Scintillation photons hitting the photocathode liberate electrons through the photoelectric effect, and under the impact of the electrical potential the electrons are accelerated and focused on the sequence of dynodes. The potential difference between each pair of neighboring dynodes is higher than the previous one, enabling further acceleration and finally leading to a large multiplication of the electron

flux from its initial value. Usually, the total accelerating voltage is between 500-3000 V [73]. Finally, the resultant output signal at the anode is collected and processed by appropriate electronics. The magnitude of this signal is proportional to the initial amount of electrons emitted by the photocathode.

Although PMT devices are very common for the scintilllator signal conversion, they are not EMP resistant and hence are not applicable to high-intensity laser-plasma experiments.

CCD camera

A CCD is a digital camera system. In the case of CCD coupling, the scintillator is placed on the detecting area of the camera and the images are captured. The images consist of numerous frames and are stored in a proprietary event record format, which separates each frame to allow for image processing. The image format records the x-position, y-position and signal level for each pixel in the frame, enabling further signal reconstruction. For further information see [74], [75] and references therein.

The main advantage of CCD cameras in the laser-plasma experimets is that they are EMP resistant. These devices also show high spatial resolution, low noise level, and wide dynamic range.

Chapter 4

Simulations of high-energy photon interaction with a detector

Simulations are a common tool not only for general understanding and predictions of complex physical phenomena, but also for development and examination of different diagnostics before being employed in experiments. The main advantage of such method is that it permits to investigate different design configurations of a particular diagnostics and to study its interaction with particles and radiation prior to its construction, making the design more economical and faster.

Monte Carlo (MC) method is one of the possible simulation approach. The MC calculations are based on a repeated random sampling and its subsequent statistical interpretation, allowing to model complex situations where many random variables are involved. The technique was developed in the 1940s within the Manhattan Project [76]. In particle physics, the MC method is able to simulate particles transport and interactions with media, creating primaries and tracking them together with the secondaries, applying the physics of collision processes.

In this chapter, principles of the MC based code FLUKA, which was used for the development and tests of a novel detector (see Chap.5), are briefly described, as well as a general idea of the FLUKA simulation setup.

4.1 Principles of the FLUKA code

FLUKA (FLUktuirende KAskade) is a fully integrated input-based particle physics Monte Carlo simulation code, the history of which dates back to 1970's. As of today, the code is jointly developed by INFN (Istituto Nazionale di Fisica Nucleare) and CERN (European Organization for Nuclear Research)[77, 78]. FLUKA serves as a general purpose tool for calculations of particle transport and interactions with matter and is used world-wide. A wide range of possible applications are covered by this tool, including proton and electron accelerator shielding, target design, calorimetry, activation, dosimetry, detector design, cosmic rays and radiotherapy. Furthermore, FLUKA is able to manage high-accuracy simulations of about 60 different particles with energies ranging from hundreds of eV up to thousands of TeV.

Such high accuracy simulations are possible due to the implementation and improvement of sound and modern physical models in the FLUKA code: microscopic models

are adopted whenever possible, consistency among all the reaction steps and/or reaction types is ensured, conservation laws are enforced at each step, results are checked against experimental data at single interaction level. For this reason, final predictions are obtained with a minimal set of free parameters fixed for all combinations of energy, target and projectile, even if no experimental data are yet available for a particular combination.

For each kind of particle, a set of corresponding effects accompanying its transport and interaction with matter is considered. Moreover, this applies for all the generated secondaries which are tracked down as long as their energy exceeds the transport limit (set manually or automatically). In the case of electrons and photons, FLUKA manages all the interactions and scattering processes, including those described in Chap. 2. It is possible to track also charged particles motion, even in the presence of magnetic field.

Apart from providing comprehensive physical models, FLUKA is able to create and handle very complex geometries using a Combinatorial Geometry (CG) approach. The CG relies on elementary and complex objects. The elementary ones are defined as convex solid bodies, infinite cylinders and planes, while the complex objects (called regions) are defined as combinations of elementary bodies obtained by boolean operations: Union, Subtraction and Intersection. Whichever material required by the user can be defined in FLUKA. Subsequently, any material can be assigned to any created region.

Taking into account the radiation field and the material geometry described by the user, FLUKA is routinely used to make predictions of the expectation value of one or more quantities. For such a purpose, different estimators are available which score the quantity of the interest (see next section). Among the most commonly scored quantities are dose, fluence, energy deposition, current, track length, etc.

The FLUKA code is developed using the Fortran-77 language. However, for most applications programming is minimized for the user. Nevertheless, a number of Fortran routines can be developed by the user in the case of special requirements.

4.2 Simulation setup in FLUKA

To set up a FLUKA simulation, the input file must be firstly created. Such a file consists of a series of instructions (named cards). The input file typically contains the following sections:

- Title and comments;
- Description of the problem geometry: bodies and regions;
- Definition of the materials;
- Material assignment: correspondence material-region;
- Definition of the particle source, its origin, energy and direction;
- Number of primaries to be simulated;
- Definition of the requested "detectors" (estimators) to calculate the expectation value of the physical quantities;

- Definition of biasing;
- Definition of physics settings such as energy cut-offs, step size, physical effects to be deactivated, etc.

The "standard input" is an ASCII file with extension .inp. However, it is also possible to create the input file using Flair (FLUKA Advanced Interface): an advanced user-friendly graphical interface developed using Phython programming language [79]. Flair's purpose is to facilitate the editing of the FLUKA input files, execution of the code and visualization of the results. The functionality of the interface includes, inter alia: i) an interactive geometry editor, ii) debugging, compiling, running and monitoring of the status during a run, iii) post processing of the results, iv) visualization and plotting of the results.

To score the different aforementioned quantities, specific cards should be introduced and adjusted. One of the most used scoring options is a USRBIN card, which is the most relevant card for the study described further in this thesis. USRBIN provides detailed space distribution of one or several quantities (e. g. energy deposition, fluence), calculating and scoring it in a regular binning structure. Such structure is a grid created by dividing the region of the interest into a number of equal subzones called bins and is geometry-independent (does not need to coincide with any geometry region). Bin scoring is based on simple integer arithmetic. Usually, increasing the number of bins can lead to more precise scoring, but too small bin dimensions can significantly slow down the calculation process.

The results from USRBIN are normalized per unit volume and per unit primary weight. By means of Flair or some other suitable graphics package, the USRBIN output can be presented in the form of color maps.

The output of the FLUKA run is contained in a binary or text form. For the data processing via other than Flair application, there is a need to convert binary files into other extension (e.g. .txt). For this task, the use of a dedicated ancillary fortran program is required. Obtained data can be further processed using any appropriate software: Matlab, C++, Python-based applications, etc.

Using FLUKA, it was possible to model the initial design of the novel electromagnetic calorimeter that is described in details in the next chapter. To give an example of the FLUKA geometry, the calorimeter design is shown in Fig. 4.1: as it can be seen, it consists of two regions of different materials. The detector's interaction with an incident photon beam was simulated and the energy deposition was scored along the calorimeter length using a USRBIN card. An illustration of the USRBIN scoring in such a device is shown in Fig.4.2. The photon beam incident on the device is characterized with the MB temperature T = 10 MeV. The colorbar is in logarithmic scale.

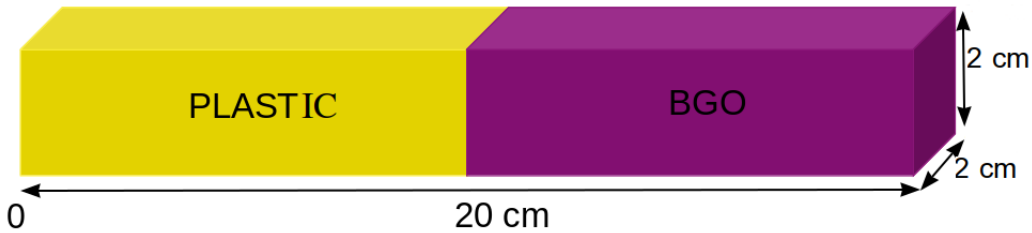

Fig. 4.1. An example of the FLUKA geometry, showing the initial design of the electromagnetic calorimeter which consists of two different materials.

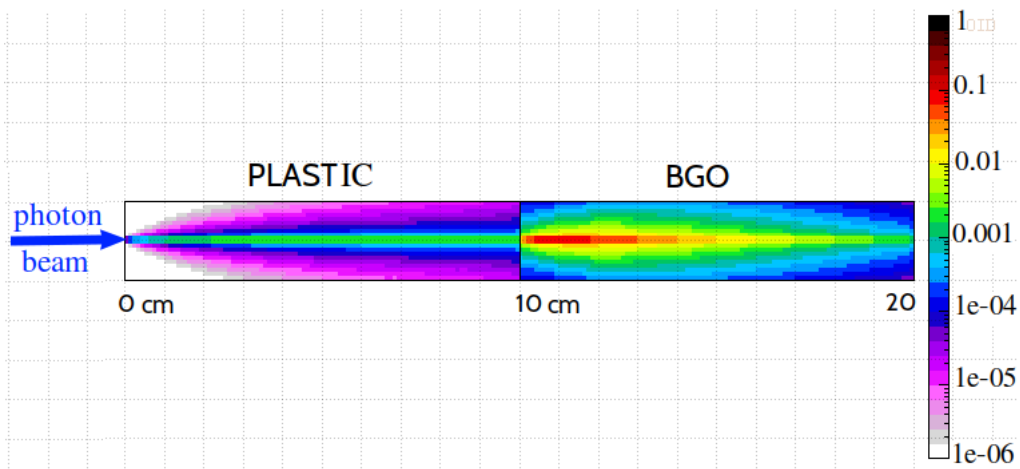

Fig. 4.2. An example of the USRBIN scoring, showing the energy deposition in the calorimeter ([GeV/cm^3/primary], logarithmic scale).

Chapter 5

Development of a novel electromagnetic calorimeter for the detection of high-energy photons

In this chapter the development of the high-energy photons detector is described, and the progress is summarized. The project is a collaboration between ELIMAIA and Monte Carlo groups from ELI Beamlines laser facility.

Since high repetition rate petawatt lasers with intensities exceeding 10^{21} W/cm^2 will be employed during the upcoming ELIMAIA experiments, very intense gamma-ray bursts with femtosecond duration will be produced during laser-matter interactions (with expected temperatures up to 50 MeV). As it was mentioned in Chap. 3, the currently available diagnostics are not suitable for spectroscopy of such intense and short photon bursts, therefore there is the need for a new type of detector. The required device should satisfy several criteria. The most important ones are the following: first, the detector has to be an active one, and second, it has to provide quality information about the energy spectrum of the incident photons. Furthermore, the detector should be relatively compact in order to be portable and cost-effective, and not be affected by the EMP coming from the laser-matter interaction.

The choice of the detector fell on an electromagnetic calorimeter based on scintillators, as such device meets the required criteria the best.

It has been observed, that in laser-plasma experiments the bremsstrahlung photon spectrum consists of at least two MB energy distributions [80, 81], one with high temperature (tens of MeV), caused by the hot electrons, and one with low temperature (hundreds keV), caused by the so called cold electrons. In that regard, it was decided to use two different scintillating materials in the calorimeter setup to be able to measure both the high and low-energy components. Furthermore, given the large amount of photons expected, the calorimeter designing approach was agreed to be different from common arrangements (described in section 3.2): the device consists of solely scintillators that serve as absorbers and detectors of the radiation at the same time.

Multiple Monte Carlo simulations of the interaction between the detector and the photons of a wide range of temperatures were performed in FLUKA. In order to determine the two temperatures present in the photon spectrum, a signal unfolding technique was developed on grounds of the Monte Carlo simulations results. Subsequently, the unfolding technique was applied on different calorimeter setups, resulting in the optim-

ization of the initial design. Furthermore, the calorimeter is being optimized as regards scintillating materials used.

This chapter introduces the initial calorimeter design and the simulation setup. This is followed by the description of the implemented unfolding algorithms, along with the consequent design optimization. Finally, results, next steps, and related issues are summarized in discussions.

5.1 Initial design and simulation setup

The calorimeter was modeled in 3D using the FLUKA graphical interface Flair (see Chap. 4). The focus was laid on a simple initial design and simulation setup as a starting point. The design was simplified to avoid modeling details unnecessary for studying the photon-scintillator interactions (e.g. readout electronics, background noise shielding, etc.) and consider only the core of the detector, i.e. scintillators. The medium surrounding the detector was set as vacuum to eliminate interactions outside of the device. The radiation source was emitting photons following the two-temperature MB spectrum in a form of a pencil beam (non-divergent and point-like) along the calorimeter axis. Such simplifications imply not only the acceleration of the modeling process, but also of the simulation process, because the computational time increases with more sophisticated simulation setups.

With regard to the expected two-temperature photon distribution, two different scintillating materials were chosen to constitute the device: plastic (EJ-200 [82]) and BGO (see Section 3.2).

The density of plastic scintillators is low enough (1.03 g/cm^3), thereby such crystals are able to resolve the low energy component of the incident radiation. On the other hand, the BGO scintillator is of high density (7.13 g/cm^3) and high atomic number, which makes it possible to detect also high-energy photons. Therefore, it was decided to use plastic scintillators to form the front part of the calorimeter to stop the low-energy photons. The high-energy component, barely affected by plastic, will be stopped in the BGO material, constituting the remaining part of the device.

In the initial design, the calorimeter is divided into two equal parts of the aforementioned scintillators. The total length of the detector was set as 20 cm (each scintillator is of 10 cm), the width and height as 2 cm each. A calorimeter of such dimensions was considered as compact enough to be used in the experiments and at the same time effective to contain the major part of the electromagnetic cascade. A visualization of such design was presented in the previous chapter in Fig. 4.1.

To score the deposited energy, the calorimeter was divided into 200 equal bins along its length which imitate 1 mm thick scintillator layers. The first layer is the one closest to the incident radiation.

The interaction with the calorimeter of photons having MB temperatures in the range 100 keV - 40 MeV was simulated in FLUKA. The upper bound of the range is given by the hot electrons temperatures estimated in section 1.2.3, assuming the maximum temperature of photons is equal or less than that of the hot electrons. An example of the source energy spectrum with T = 20 MeV is shown in Fig. 5.1. As it can be seen, some photons from such distribution can reach energies more than 140 MeV.

The simulations confirmed, that the detector dimensions are sufficient to contain

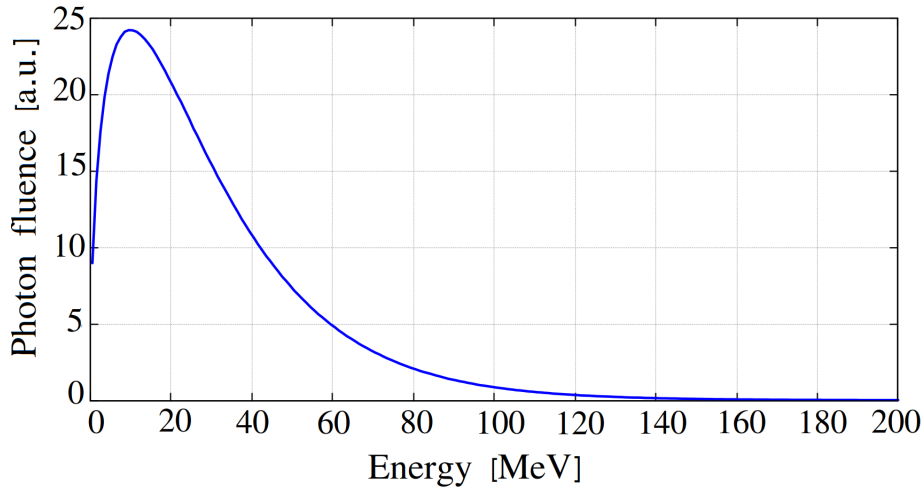

Fig. 5.1. Source energy spectrum of a the Maxwell-Boltzmann distribution with $T = 20$ MeV.

the major part of the electromagnetic shower. The energy deposited by photons of 20 MeV temperature in the calorimeter is presented in Fig. 5.2.

Resting on the initial design, the unfolding algorithm was developed; it is described in the following section.

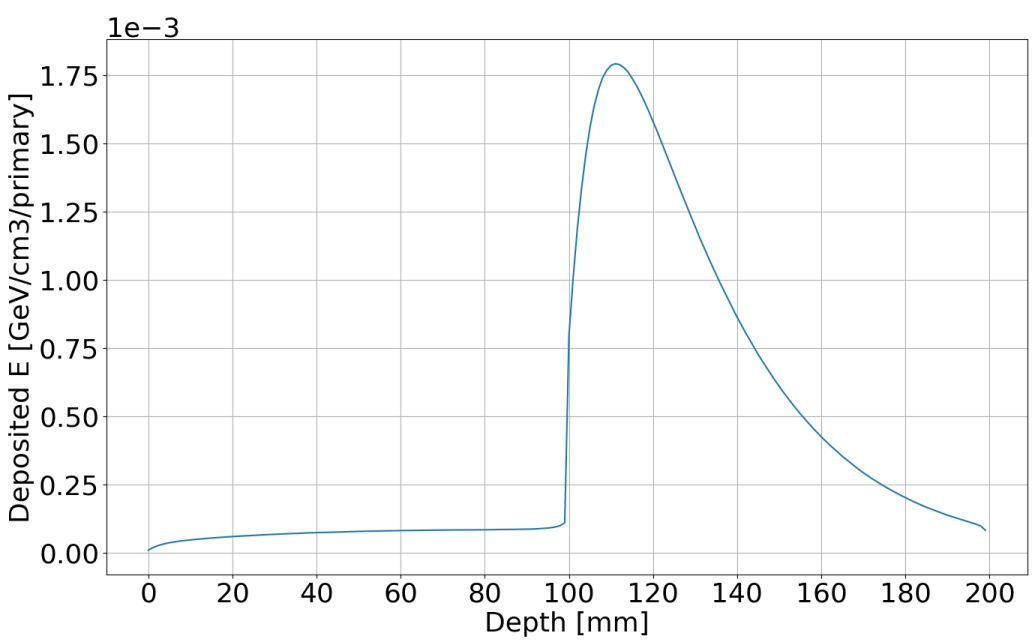

Fig. 5.2. Energy deposition in the initial design for a T = 20 MeV MB distribution, [GeV/cm^3/primary]

5.2 Development of the unfolding technique

5.2.1 Necessity of the unfolding

In order to proceed from the experimentally measured calorimeter signal to the physical quantities, such as photons energy distribution, a method for the signal reconstruction should be developed. In that regard, the attention was drawn to the ratios of the energy deposited in two adjacent calorimeter layers (bins), denoted as E_i+1/E_i, where i is number of the layer. The dependence of several ratios on the photons spectra was studied and is presented in the following figures.

As it can be seen from the Fig. 5.3, the largest rise in the deposited energy is on the border plastic-BGO, which is between bins 100 and 101; also, the ratio E_101/E_100 increases monotonically and sharply with the simulated temperatures (x-axis) in comparison to other ratios. It indicates that theoretically we could resolve the initial photon temperature distribution by measuring mainly this ratio and comparing it with the simulations results. Indeed, in the case of the one-temperature photon distribution with T=50 MeV presented in the figure, all of the ratios indicate the same photon temperature, corresponding to the one used as input.

However, as it is clear from Fig. 5.4, when two-temperature photons distribution with T = 10 MeV + 100 MeV is considered, every measured ratio (dotted lines) indicates different temperature making it impossible to identify the input temperature of the photons.

Therefore, a different approach for the evaluation of the photon energy distribution was needed, and the choice fell on the development of an appropriate unfolding technique.

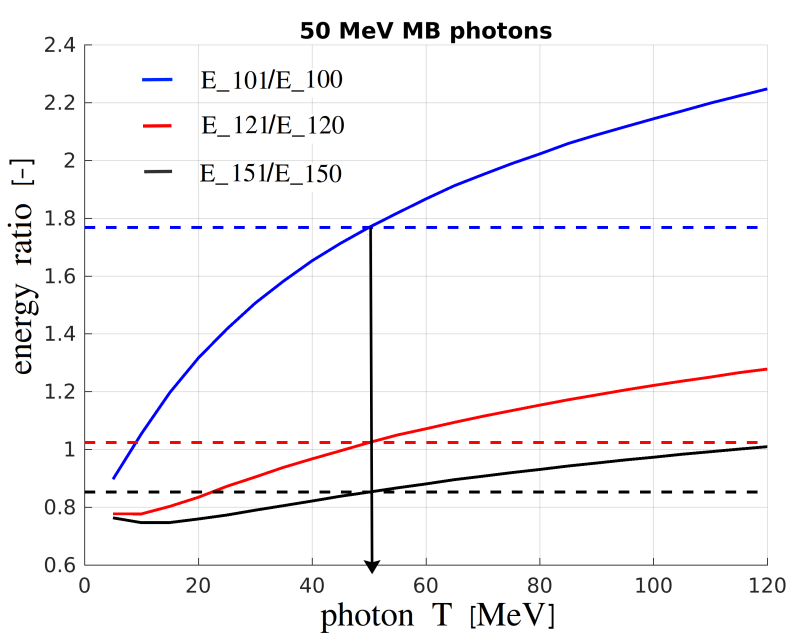

Fig. 5.3. Ratios of the energy deposited in several calorimeter's layers as function of the photons temperature. When exposed to one-temperature radiation with T = 50 MeV, all the ratios (dotted lines) indicate the same temperature of the photon beam correctly.

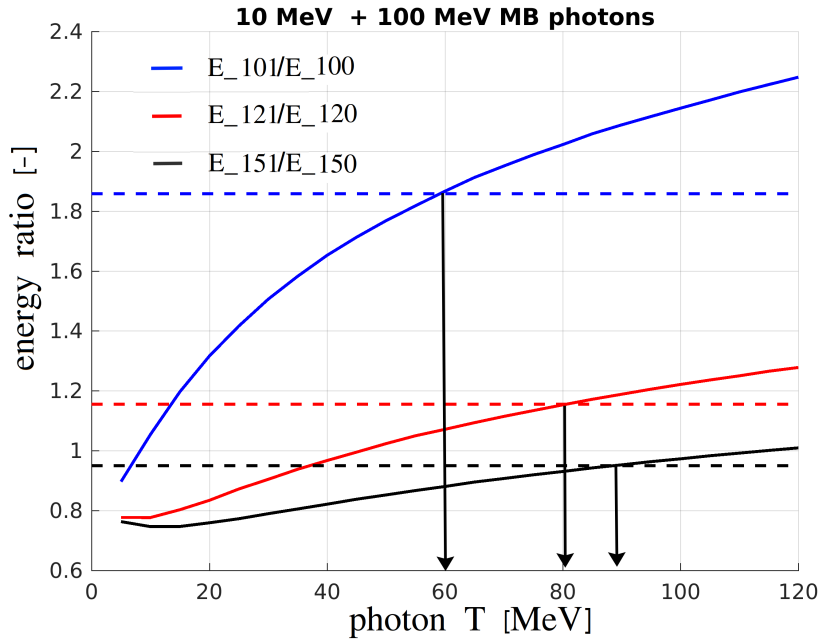

Fig. 5.4. Ratios of the energy deposited in several calorimeter's layers as function of the photons temperature. When exposed to two-temperature radiation with T = 10 MeV + 100 MeV, every ratio (dotted lines) indicates different temperatures of the photon beam.

In signal processing, a signal unfolding is a reconstruction of some original undistorted physical quantity based on detector's response. The unfolding can be implemented using different methods depending on the detector and the measured quantity. In our case we need to unfold energy distribution of the incident photons proceeding from the longitudinal distribution of the energy deposited within the calorimeter layers.

The unfolding technique requires:

– to determine a response matrix based on the performed simulations,

– to develop the unfolding algorithm.

We implemented and tested two possible unfolding algorithms; however, only one appeared to be functional for our case.

5.2.2 Gaussian elimination with pivoting

On the basis of the performed simulations, it is possible to create a so called *calorimeter response matrix* $\boldsymbol{R} \in \mathbb{R}^{m \times n}$ (Eq.(5.1)), where m is the number of layers in which energy deposition was scored along the calorimeters length and n is the number of the simulated photons MB temperatures. The temperatures used are marked as $T_1,\ T_2, ...,\ T_{max}$. Therefore, the response matrix contains values of the energies deposited in each bin i

when exposed to a MB spectrum of photons with temperature T_j:

$$\boldsymbol{R} = (r_{i,j}) = \begin{pmatrix} r_{i=1,T_j=T_1} & r_{i=1,T_j=T_2} & \cdots & r_{i=1,T_j=T_{max}} \\ r_{i=2,T_j=T_1} & r_{i=2,T_j=T_2} & \cdots & r_{i=2,T_j=T_{max}} \\ \vdots & \vdots & \ddots & \vdots \\ r_{i=m,T_j=T_1} & r_{i=m,T_j=T_2} & \cdots & r_{i=m,T_j=T_{max}} \end{pmatrix} \tag{5.1}$$

Let s_i be the energy deposited in the layer number i. A vector $\boldsymbol{s} \in \mathbb{R}^m$ then represents the deposited energies in each calorimeter layer.

Assuming that vector $\boldsymbol{s}$ is a signal measured by the detector and $\boldsymbol{x} \in \mathbb{R}^n$ is a vector containing weights of the MB temperatures presented in the incident photon beam, it is possible to formulate the unfolding problem as a search of the solution of the following system of linear equations:

$$\boldsymbol{R} \cdot \boldsymbol{x} = \boldsymbol{s} \tag{5.2}$$

The solution, i.e. the vector $\boldsymbol{x}$, can be found using the Gaussian elimination algorithm with pivoting [83] (in our case, Matlab software was used for this task).

To check the reliability of the introduced method, the Eq.(5.2) was solved using a test vector $\boldsymbol{s}$ combined of two MB temperatures (10 MeV a 20 MeV) with different weights:

$$s_i = 7r_{i,T=10} + 3r_{i,T=20} \ , \tag{5.3}$$

where $r_{i,T=10}$ and $r_{i,T=20}$ are elements of the response matrix representing energy deposited in i-th bin by 10 MeV and 20 MeV photon beam, respectively.

A representation of the solution vector $\boldsymbol{x}$ for this case is shown in Fig. 5.5. The x-axis depicts all the temperatures present in the response matrix and the y-axis indicates their reconstructed weight. An ideal case is shown on the left, with no noise added to the artificial calorimeter response (vector $\boldsymbol{s}$). As can be seen, the unfolding algorithm evaluated the input temperatures and their weights correctly, showing two distinctive peaks of different height.

The right plot depicts the solution vector in the case when a small noise was included to the calorimeter response by addition of a random number from the Gaussian distribution randg$(\mu = 0, \sigma = s_i)$ to each vector element (signal-to-noise ratio is 10^{-4}):

$$s'_i = s_i + 10^{-4}\text{randg}(\mu = 0, \sigma = s_i) \tag{5.4}$$

where s'_i denotes the signal with added noise . As it can be seen from the figure, the unfolding output is indiscernible which indicates that the unfolding algorithm is no longer reliable. Although the added noise is very small, deviations are significant and it is difficult to distinguish the peaks. In reality, the signal-to-noise ratio of the detector is expected to be much higher than the mentioned value (due to the light output fluctuations, electronic noise, etc.). Therefore, the use of the Gaussian elimination unfolding algorithm was ruled out.

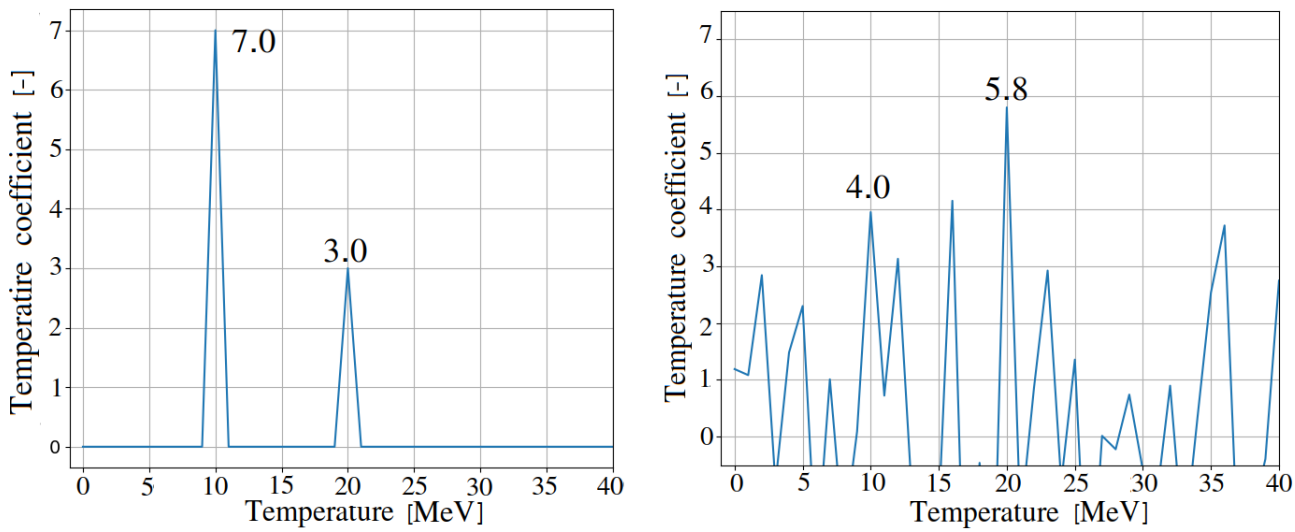

Fig. 5.5. Gaussian unfolding of the calorimeter signal after the interaction with a photon beam combined of 2 MB functions: left - without noise, right - with noise.

5.2.3 Gradient unfolding method

The second unfolding technique tested relies as well on the response matrix from Eq. (5.1). However, as distinct from the first technique, an interpolation between the matrix points using cubic splines is implemented. The interpolation function $f(i, T_j)$ is then able to provide energy deposition in layer number i for any $T_j \in [T_1,\ T_{max}]$, without being limited to only a finite number of simulated temperatures.

Conventions

It is considered, that the source simultaneously emits two groups of photons, N_1 photons with the MB temperature T_1 and N_2 photons with the MB temperature T_2, where N_1 and N_2 represent total numbers of the photons in each group. Since $f(i, T_j)$ is the energy deposition per primary particle, the signal in layer i can be calculated as

$$s_i = N_1 \cdot f(i, T_1) + N_2 \cdot f(i, T_2) \tag{5.5}$$

The aim of the unfolding program is to determine four parameters $N_1,\ T_1,\ N_2$ and T_2 which characterize the radiation, using the the vector $\boldsymbol{s}$ and the function $f(i, T_j)$.

The unfolding program uses guessed detector responses, calculated from an initial guess of the parameters $\overline{N_1},\ \overline{T_1},\ \overline{N_2}$ and $\overline{T_2}$:

$$\overline{s}_i = \overline{N_1} f(i, \overline{T_1}) + \overline{N_2} \cdot f(i, \overline{T_2}) \tag{5.6}$$

The difference between the true calorimeter response $\boldsymbol{s}$ and the guessed response $\overline{\boldsymbol{s}}$ is defined as:

$$\chi^2(\overline{N_1}, \overline{T_1}, \overline{N_2}, \overline{T_2}) = \sum_{i=1}^{n} (s_i - \overline{s_i})^2 \ \geq 0. \tag{5.7}$$

The aforementioned function indicates how close to the measured parameters the guess is. If the guess is correct, the difference between $\boldsymbol{s}$ and $\overline{\boldsymbol{s}}$ equals zero, i.e.:

$$\left(N_1 = \overline{N_1} \wedge T_1 = \overline{T_1} \wedge N_2 = \overline{N_2} \wedge T_2 = \overline{T_2}\right) \Longleftrightarrow \chi^2 = 0 \tag{5.8}$$

Therefore, the goal of the unfolding program is to minimize the χ^2-function.

Unfolding program description

The unfolding code consists of two consecutive algorithms aiming to minimize the χ^2-function (Eq.(5.7)):

1. In the first algorithm, a user firstly selects a grid for the parameters $N_1,\ T_1,\ N_2$ and T_2: a minimum, a maximum and a desired amount of points in between. After that, using simulated values from the response matrix created beforehand, the program calculates the χ^2-function for all possible combinations of the selected parameters. Eventually, it returns the one for which the χ^2-function is minimal.

2. The combination from the first step is then used as a starting vector $\boldsymbol{x} = (N_1, T_1, N_2, T_2)$ for the second algorithm - the gradient unfolding. This algorithm is based not only on the calculations of the χ^2-function, but also its gradient which allows to determine the direction of the function's strongest decrease and subsequently move the starting vector in this direction:

$$\boldsymbol{x'} = \boldsymbol{x} - \alpha \cdot \Delta\chi^2, \tag{5.9}$$

   where α determines the distance the starting point should travel to reach the minimum as close as possible. Based on the new parameters, a new value of the χ^2-function can be calculated and the process repeats. Therefore, the algorithm is able to perform further minimizations of the χ^2-function, reaching more precise values of the parameters $N_1,\ T_1,\ N_2$ and T_2.

   An intuitive explanation of the gradient unfolding algorithm for the case of one-temperature signal $s(i) = 40 \cdot f(i, T_{20})$ is presented in Fig. 5.6, showing the dependence of the χ^2-function on the parameters N_1 and T_1: the function values are minimal in the vicinity of the $N_1 = 40$ and $T_1 = 20$.

A scheme of the entire unfolding program is shown in Fig. 5.7. The two described algorithms are circled in red. A user input comprises a grid for the parameters of interest for the first algorithm, a calorimeter signal and a number of iterations to be used in the second algorithm.

It is worth mentioning why the two algorithm were used in combination, whilst in principle they could perform the unfolding individually. The idea of the first algorithm is very simple and reliable; however, when employed singly, it is extremely time consuming. At the same time, the gradient unfolding is faster and more accurate, but strongly depends on the starting point: the unfolding can stop at some local minimum of the χ^2-function, not the global one we are interested in. Therefore, the most suitable solution is to make a first approximation by the first technique and then use it as a starting point in the second one.

The unfolding code was written using Python language.

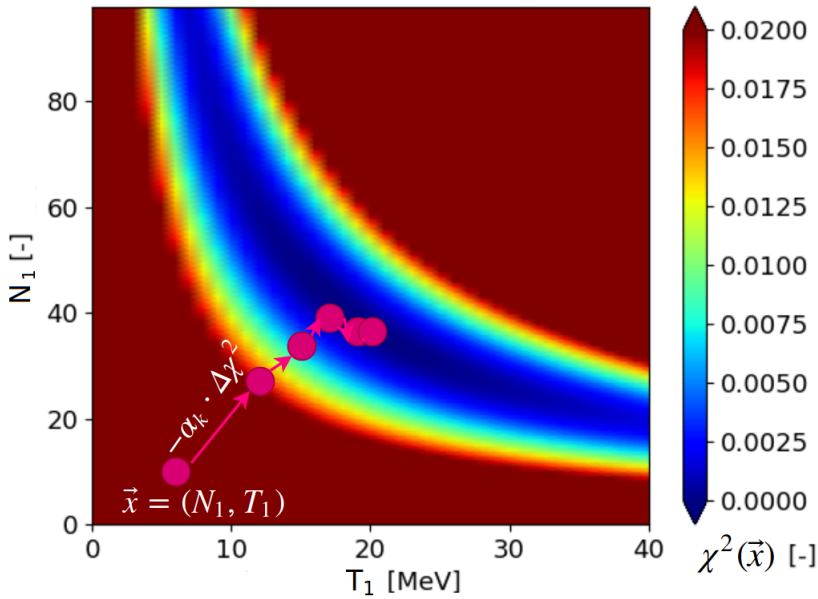

Fig. 5.6. An illustration of the gradient unfolding algorithm for the case of one-temperature signal (first five iterations). Values of the χ^2-function depending on the parameters N_1 and T_1 are presented in colour. The unfolding starts at random point and quickly proceeds in the direction of the function's minimum.

Accuracy

The accuracy of the unfolding program is described by means of the relative error of each parameter, which indicates how the unfolded result x_{unf} differs from the true values x_{true}:

$$\delta_x = \frac{|x_{true} - x_{unf}|}{x_{true}} \cdot 100\% \qquad \text{for } x = N_1, T_1 N_2, T_2, \tag{5.10}$$

Noise definition

After preliminary tests of the unfolding program, a high level of accuracy was reached ($< 0.1\%$). However, a real experimental signal will be affected by noise and the unfolding code should be resistant to it. Three parameters can typically cause the noise in calorimeters, as described in section 3.1.3. Yet one is anticipated to produce the most significant noise in our case. This is the scintillator light output noise, which is proportional to the square of the deposited energy.

Assuming that $s(i)$ is the energy deposited in layer i per primary particle (Eq. (5.5)), the noise can be defined as:

$$s'_i = s_i + \text{randg}(\mu = 0, \sigma = \beta) \cdot \sqrt{s_i} \tag{5.11}$$

Where $\text{randg}(\mu = 0, \sigma = \beta)$ denotes a random number from the Gaussian distribution. The variance σ, determining the level of the noise, was estimated based on the FWHM (Full Width Half Maximum) of the BGO scintillator as $\sigma = \beta = \sqrt{1\text{keV}}$. The magnitude of such noise is approximately 10% of the signal in bin i.

In the next section the functionality of the gradient unfolding algorithm will be demonstrated.

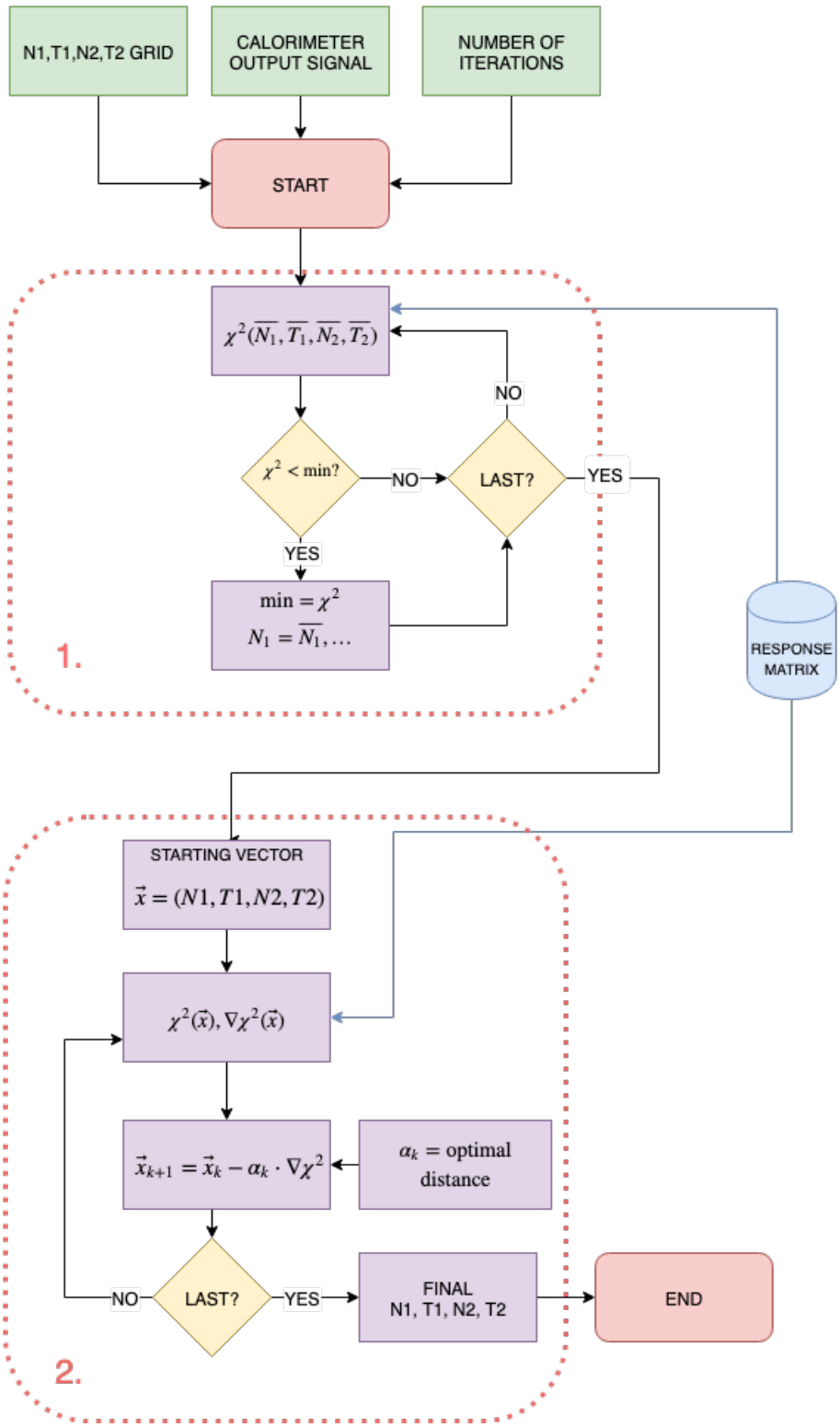

Fig. 5.7. A scheme of the developed gradient unfolding technique, consisting of two consecutive algorithms.

5.3 Design optimization

The initial design of the calorimeter has undergone the preliminary optimization of the used materials, as well as the preliminary geometry optimization, in which the developed unfolding technique was tested.

5.3.1 Material optimization

To compare the calorimeter output when different materials are used, a PWO scintillator was tested as the dense part of the calorimeter. Commonly, the PWO is typically employed for high-energy measurements [84] due to the highest density of 8.23 g/cm^3. Even if the PWO is a more expensive material and produce less light output that the BGO, the comparison of the energy deposition effectiveness was of interest. Therefore, a number of simulations was performed testing the PWO and BGO in the calorimeter setup when exposed to similar radiation. The comparison of the energy deposition peak in each scintillator for different photon temperatures is shown in Fig. 5.8. Although the density of the BGO is slightly lower than that of the PWO, it does not significantly influence the position of the energy deposition peak in the calorimeter even for extremely high photon temperatures, as can be seen from the figure. Based on this fact, the BGO was kept as the dense part of the calorimeter.

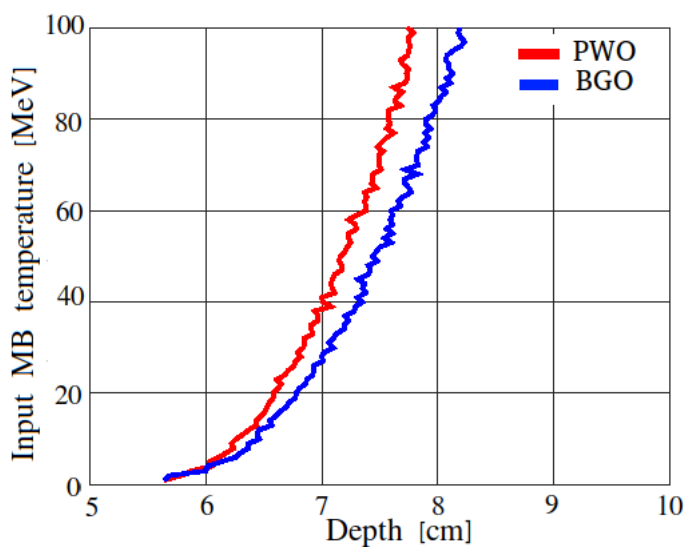

Fig. 5.8. Dependence of the energy deposition peak in the PWO (red) and BGO (blue) layers on the input photon temperatures in the range 1 - 100 MeV.

5.3.2 Geometry optimization

By means of the implemented unfolding code it is possible to optimize the calorimeter's geometry. The optimization is required to approach a more realistic and efficient configuration as regards thicknesses of the plastic and BGO parts and number of layers, for which the accuracy of the unfolding program will be maximized.

The geometry tests are based on the simulations of the photons interaction with a particular design configuration and the subsequent unfolding with noise added to the signal.

The response matrix used in the unfolding was created using the results of 48 simulations performed in the following range of the photons temperatures:

- 100 keV - 1 MeV, step 50 keV
- 2 MeV - 20 MeV, step 1 MeV
- 22 MeV - 40 MeV, step 2 MeV

During the unfolding procedures, the artificial signal from the calorimeter was set arbitrarily according to Eq. (5.5) as

$$s(i) = 5.1 \cdot f(i, 210\text{keV}) + 1.1 \cdot f(i, 21\text{MeV}), \tag{5.12}$$

containing a low-energy and a high-energy photons part for the reasons discussed in the previous text. It is noteworthy, that the temperatures used in Eq (5.12) are intentionally not contained in the response matrix to make the test of the unfolding more challenging.

Different number of iterations of the unfolding algorithm was examined in the range 500 - 13000. Typically, the increasing iterations number is proportional to the accuracy and to the program execution time. However, after a certain amount of iterations the unfolding results appeared to be close to the true value and further improvement is unnecessary. As a compromise between the accuracy and time, the number of iterations was eventually set as 3000, because it has proven to be sufficient for the unfolding and at the same time took it only 3 minutes to finish. Fig. 5.9 shows the rapid minimization of the χ^2-function value depending on the iteration number of the unfolding.

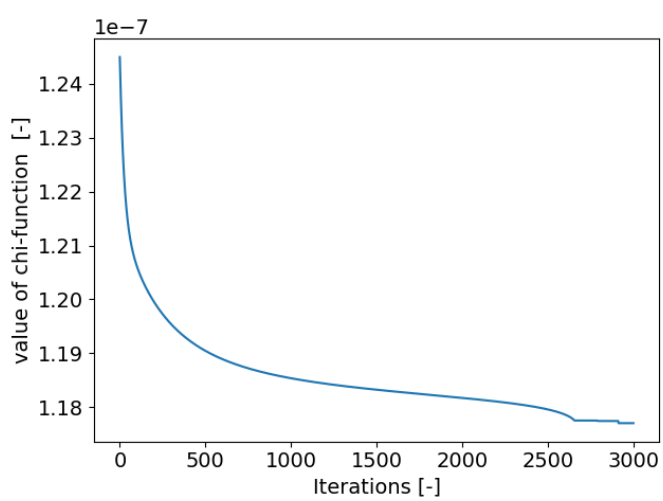

Fig. 5.9. Minimization of the χ^2-function value depending on the iteration number of the unfolding.

An example application of the aforementioned proceeding for the case of the initial geometry configuration is described in the following text. Given the small size of the simulated bins (1 bin = 1 mm), it has been possible to re-sum bins together, in order to imitate a more realistic thicker physical bin. The manufacturing of the 1 mm bin is more expensive and, in this case, also unnecessary, as proved by the following studies. Different rebinnings have allowed to test different geometries.

In that regard, each scintillator was consequently divided into 50, 25, 10 and 5 bins. The unfolding procedure was run and its accuracy for each of the N_1, T_1, N_2, T_2 parameters was calculated for each combination. Since the artificial noise used in the code was based on random sampling, each unfolding was performed 10 times to find a mean value of the accuracy with 10%−error.

The results of the tests, showing the accuracy of the unfolding for each parameter depending on the binning are presented in Fig. 5.10. The most accurate values are colored in green. Based on such a table, it is possible to select the most suitable binning for the tested design: for example, 25 layers of 4mm thickness of both plastic and BGO scintillators. The accuracy for each parameter in this case is the following: $\delta_{N_1} = (19.5 \pm 2.0)\%$, $\delta_{T_1} = (23.5 \pm 2.4)\%$, $\delta_{N_2} = (5.0 \pm 0.5)\%$, $\delta_{T_2} = (2.7 \pm 0.3)\%$. The second temperature is more accurate than the first, because it is 10 times higher, hence cause higher energy deposition and stronger signal and is easier to be unfolded.

N1				
Pla/BGO	50 (2 mm)	25(4 mm)	10 (1 cm)	5 (2 cm)
50 (2 mm)	8.00%	26.50%	47.60%	13.20%
25(4 mm)	14.80%	16.80%	45.20%	41.50%
10 (1 cm)	19.00%	19.50%	38.30%	50.40%
5 (2cm)	9.30%	18.00%	60.80%	59.40%

N2				
Pla/BGO	50 (2 mm)	25(4 mm)	10 (1 cm)	5 (2 cm)
50 (2 mm)	2.90%	3.40%	5.50%	2.90%
25(4 mm)	3.10%	3.60%	5.30%	4.20%
10 (1 cm)	3.40%	5.00%	3.10%	4.60%
5 (2cm)	4.90%	2.60%	5.90%	8.00%

T1				
Pla/BGO	50 (2 mm)	25(4 mm)	10 (1 cm)	5 (2cm)
50 (2 mm)	15.30%	29.90%	41.40%	22.70%
25(4 mm)	20.30%	14.40%	48.80%	46.10%
10 (1 cm)	22.80%	23.50%	38.20%	57.80%
5 (2cm)	13.60%	24.40%	65.10%	75.10%

T2				
Pla/BGO	50 (2 mm)	25(4 mm)	10 (1 cm)	5 (2 cm)
50 (2 mm)	2.50%	2.40%	4.80%	2.20%
25(4 mm)	3.10%	3.30%	6.60%	4.40%
10 (1 cm)	4.00%	2.70%	4.10%	6.00%
5 (2cm)	4.60%	3.20%	6.10%	7.80%

Fig. 5.10. Comparison of different rebinnings of the scintillators in the calorimeter setup. A mean accuracy of the unfolding for each parameter in each combination is presented. Relative error is 10% of the mean value.

.

5.4 Discussions of the results

The performed simulations have shown, that the electromagnetic calorimeter with dimensions of 2cm×2cm×20cm composed of two different scintillators is suitable for the measurements of the photon energy spectrum of the two-temperature MB distribution in the range (100 keV, 40 MeV). Such dimensions are appropriate regarding not only compactness and portability of the detector, but also cost-savings at the production

step. Due to its compactness, such detector can theoretically be inserted even inside the target chamber close to the interaction area, if required.

Two different unfolding techniques were developed. The unfolding technique based on the Gaussian elimination algorithm works correctly under ideal conditions, but collapses when a small amount of noise was considered. The reason is that the system of equations is underdetermined (fewer equations than unknowns).

On the other hand, the gradient unfolding technique has proved to work correctly not only under ideal conditions, but also with the presence of artificial noise added to the detector response. Moreover, the unfolding procedure is completed within a short time (< 5min) that enables to work in high-repetition rate and is sufficiently accurate.

As regards scintillating materials, the simulations have proved the effectiveness of plastic and BGO for the measurement of the low and high energy component of the photons. Additionally, these scinitillators are widely available from the production perspective. The BGO scintillator was deemed more appropriate than the commonly used for high-energy measurements PWO one, as it produces more light while being almost as dense as PWO. However, other potential materials are also taken into account: their essential parameters are presented in the table below. High light yield implies better signal and high density enables to detect photons of high energy within small distances. The study of the use of different materials is ongoing.

Scintilator	Density [g/cm^3]	Light Yield [#/MeV]
BGO	7.13	8 000
CsI	4.51	41 000
LuAG:Ce	6.73	25 000
Plastic	1.06	9 000
PWO	8.23	100
YAG:Ce	4.57	30 000
YAP:Ce	5.37	25 000

Table 5.1: Possible materials to be used in the calorimeter setup.

Apart from the material optimization, the geometry optimization of the initial calorimeter design was also taken into account. During that procedure, the gradient unfolding was tested and proved to be an efficient discriminating tool. Presently, tests of different geometry setups are ongoing.

5.5 Future steps

Next steps for the calorimeter realization can be divided into the following categories:

1. For the first prototype:
   - Manufacturing of the scintillating crystals.
     Manufacturing companies have already been contacted.
   - Readout.
     To make the device resistant to the EMP coming from the laser-plasma

interaction, CCD camera will be used as a light detector (see Section 3.2.1) in the calorimeter setup. Another possible solution is to transport the light signal to processing electronics via long light guides or wave-length shifters; however, the signal in this case could be considerably reduced.

- Engineering the design.
  Moving from a simulated ideal detector would require a relevant engineering work to take care of the assembly. Engineers have already been contacted.

2. For the final design:

   - Optimization of the design.
     Different combinations of scintillators thicknesses and number of layers should be studied.
   - Optimization of the software.
     Further optimization of the algorithm should be considered in future. It mainly concerns a computation acceleration and the program expansion on multi-temperature unfolding.
   - Studies of further materials and their tests in simulations.
   - Studies of the connected physical effects.
     So far only bremstrhalung photons are considered to be measured. Nonetheless, with the increase of the laser intensity, Compton photons (described in Section 2.1) may also come into play; that would cause the third temperature in the photons energy spectrum.
   - Background effect.
     Influence of the background noise caused by photons experiencing backscattering and also from other particles coming from the source should be studied and included in further simulations.

The common final point for the first prototype and the final design is the device calibration and tests in experiments. The data obtained with the help of the calorimeter will certainly clarify some of the mentioned issues, because at present there is a lack of the experimental data in the field of high-energy photons generated from laser-plasmas.

Conclusions

The main goal of the thesis is to contribute to the development of a novel type of diagnostics for measuring high-energy photon radiation from the laser-plasma interactions, particularly to develop a signal unfolding technique. Such a device should be capable to estimate the temperature of the generated photons and to provide their energy distribution. The detector is intended to be used in the future experiments of the ELIMAIA project at ELI-Beamlines. The progresses that have been made are summarized in this thesis.

After the consideration on possible photon detectors, an electromagnetic calorimeter based on several layers of different scintillators was chosen for the photon measurements. Such a detector satisfies all the required criteria: (i) it can provide an immediate feedback on the experiment and thereby work in online regime; (ii) it can be compact and portable and (iii) it can provide a quality photons energy distribution.

Since the photon radiation is expected to have two MB temperatures, two different scintillating materials were chosen to constitute the calorimeter. Low-density plastic scintillators were opted for the detection of low photon energies in the front part of the device, while in the rest of it the BGO scintillators were employed, which are suitable for high-energy photons detection due to its high density.

A large number of simulations were conducted using the Monte Carlo FLUKA code to study the detector's response to the irradiation from the MB photon spectrum over a broad range of temperatures. The calorimeter length of 20 cm appeared to be sufficient for the detection of the expected radiation.

Proceeding from the simulations results, two signal unfolding techniques enabling to reconstruct the photon energy spectrum were developed. The results of the first one (based on the Gaussian elimination) were not satisfying when artificial noise was added to the signal. The second technique (the gradient unfolding) has proved to be functional, accurate, and fast even when such realistic conditions were considered.

Based on the simulations and on the unfolding algorithm, optimization of the initial calorimeter design is being performed: several configurations are being tested as regards the number of layers and their thickness. Eventually, the preliminary working design has been selected, confirming that the unfolding algorithm is suitable for our purpose.

Future plans were identified, including the remaining steps for the realization of the first prototype and of the final design.

Bibliography

[1] T. H. Maiman. Stimulated optical radiation in ruby. *Nature*, 187, pp. 493-494, 1960.

[2] C. Danson, et al. Petawatt class lasers worldwide, *High Power Laser Science and Engineering*, 3, 2015.

[3] ELI Beamlines official website, `eli-beams.eu`, accessed on 5.5.19.

[4] D. Strickland, G. Mourou. Compression of amplified chirped optical pulses, *Optics communications* 55.6: pp. 447-449, 1985.

[5] F.F. Chen. *Introduction to plasma physics*, 2nd edition, Plenum Press, New York (1984).

[6] A. Otto. Transparencies of lectures on Magnetospheric Physics, Chapter 2, 2006. Online at `http://how.gi.alaska.edu/ao/msp/chapters/chapter2.pdf`, accessed on 1.8.2018.

[7] B. Sedlák, I. Štoll. *Elektřina a magentismus*, Charles University in Prague, Karolinum Press, 2017.

[8] A. Henig. *Advanced Approaches to High Intensity Laser-Driven Ion Acceleration.* Dissertation thesis, Ludwig Maximilians University in Munich, Germany, 2010.

[9] J. F. Seely. Quantum Theory of Inverse Bremsstrahlung Absorption and Pair Production. *Laser interaction and related plasma phenomena*, Springer, Boston, MA, pp. 835-847, 1974.

[10] J. Pšikal. *Ion Acceleration in Small-size Targets by Ultra-intense Short Laser Pulses (Simulation and Theory).* PhD thesis, Czech Technical University in Prague, Czech Republic, 2009.

[11] A. Pukhov. Strong field interaction of laser radiation, *Reports on progress in Physics*, 66(1): 47, 2002.

[12] H. Daido, et al. Review of laser-driven ion sources and their applications. *Reports on Progress in Physics*, 75(5):056401, 2012.

[13] Z. Wang, et al. High-contrast 1.16 PW Ti: sapphire laser system combined with a doubled chirped-pulse amplification scheme and a femtosecond optical-parametric amplifier, *Optics letters*, 36(16): pp. 3194-3196, 2011.

[14] T. M. Spinka and C. Haefner. High-average-power ultrafast lasers. *Optics and Photonics News*, 28(10): pp. 26-33, 2017.

[15] V. Istokskaia. *Detection of Fast Ions from Laser-Generated Plasma*. BS thesis, Czech Technical University in Prague, Czech Republic, 2017.

[16] S. Atzeni and J. Meyer-Ter-Vehn. *The physics of inertial fusion*, Clarendon Press, Oxford, pp. 371–389, 2004.

[17] F. Brunel. Not-so-resonant, resonant absorption. *Physical Review Letters*, 59(1):52, 1987.

[18] Jan Kaufman. *Development of Radiochromic Film Diagnostics for Laser-Driven ion beams*. Master thesis, Czech Technical University in Prague, Czech Republic, 2015.

[19] P. Gibbon. *Short pulse laser interactions with matter: An introduction*, Imperial College Press, London, UK, 2005.

[20] S. C. Wilks, et al. Absorption of ultra-intense laser pulses, *Physical review letters* 69(9): 1383, 1992.

[21] F. N. Beg, et al,. A study of picosecond laser–solid interactions up to 10^{19} W cm^{-2}. *Physics of plasmas*, 4(2), pp 447-457, 1997.

[22] H. Chen, et al., Hot electron energy distributions from ultraintense laser solid interactions. *Physics of plasmas*, 16(2): 020705, 2009.

[23] Y. Q. Cui, et al., Laser absorption and hot electron temperature scalings in laser–plasma interactions. *Plasma Physics and Controlled Fusion*, 55(8): 085008, 2013.

[24] A. G. Mordovanakis, et al. Temperature scaling of hot electrons produced by a tightly focused relativistic-intensity laser at 0.5 kHz repetition rate, *Applied Physics Letters,* 96(7):071109, 2010.

[25] Y. Ping, et al. Absorption of short laser pulses on solid targets in the ultrarelativistic regime, *Physical review letters* 100(8):085004, 2008.

[26] L. V. Keldysh. Ionization in field of a strong electromagnetic wave, *Soviet Physics JETP-USSR*, 20(5), p. 1307, 1965.

[27] O. Klimo. *Simulations of Ultrashort-Pulse Laser Solid-Target Interactions*, PhD thesis, Czech Technical University in Prague, Czech Republic, 2007.

[28] Matthew M. Allen. *Ion Acceleration from the Interaction of Ultra-Intense Lasers with Solid Foils*. PhD thesis,University of California, Berkeley, 2004.

[29] F. Wagner, et al. Accelerating ions with high-energy short laser pulses from submicrometer thick targets. *High power laser science and engineering,* 4, 2016.

[30] L. Giuffrida, et al. Nano and micro structured targets to modu- late the spatial profile of laser driven proton beams, *Journal of Instrumentation,* 12(03):C03040, 2017.

[31] S. C. Wilks, et.al. Energetic proton generation in ultra-intense laser-solid interactions. *Physics of Plasmas*, 8:542, 2001.

[32] D. Batani, et al. "Effects of laser prepulses on laser-induced proton generation." New Journal of Physics 12(4): 045018, 2010.

[33] V. Bagnoud and F. Wagner. Ultrahigh temporal contrast performance of the PHELIX petawatt facility. *High Power Laser Science and Engineering*, 4, 2016.

[34] A. Lévy, et al. Double plasma mirror for ultrahigh temporal contrast ultraintense laser pulses, *Optics letters,* 32(3), pp. 310-312, 2007.

[35] P. C. João, et al. A 10-mJ-level compact CPA system based on Yb: KGW for ultrafast optical parametric amplifier pumping, *Applied Physics B*, 118(3), pp. 401-407, 2015.

[36] M.P. Kalashnikov, et al. Double chirped-pulse-amplification laser: a way to clean pulses temporally, *Optics letters,* 30(8), pp. 923-925, 2005.

[37] J. Itatani, et al. Suppression of the amplified spontaneous emission in chirped-pulse-amplification lasers by clean high-energy seed-pulse injection, *Optics Communications*, 148(1-3), pp. 70–74, 1998.

[38] A. Richards. *Alien vision: exploring the electromagnetic spectrum with imaging technology*, Vol. 9, Bellingham and Washington, DC: SPIE press, 2001.

[39] Y. K. Wu, Overview of High Intensity Gamma-ray Source- Capabilities and Future Upgrades, *2013 International Workshop on Polarized Sources, Targets and Polarimetry*, University of Virginia, 2013.

[40] Y. Glinec, et al. High-resolution γ-ray radiography produced by a laser-plasma driven electron source, *Physical review letters*, 94(2):025003, 2005.

[41] R. L. Clough. High-energy radiation and polymers: A review of commercial processes and emerging applications, *Nuclear Instruments and Methods in Physics Research Section B: Beam Interactions with Materials and Atoms,* 185(1-4):8-33, 2001.

[42] T. S. Lawrence, R. K. Ten Haken, and A. Giaccia. *Principles of Radiation Oncology, Principles and Practice of Oncology*, 8th ed., Lippincott, Williams, and Wilkins, Philadelphia, 2008.

[43] J. Galy, et al. Bremsstrahlung production with high-intensity laser matter interactions and applications, *New journal of Physics,* 9(2):23, 2007.

[44] A. Henderson, et. al. Ultra-intense gamma-rays created using the Texas Petawatt Laser, *High Energy Density Physics*, 12, pp. 46-56, 2014.

[45] D. Wu., et. al. Characteristics of X/γ-ray radiations by intense laser interactions with high-Z solids: The role of bremsstrahlung and radiation reactions. *Matter and Radiation at Extremes,* 3(6):293, 2018.

[46] E. B. Podgorsak, *Radiation Physics for Medical Physicists*. Berlin: Springer, 2006.

[47] Prof. Dr. P. Cattin, Transparencies of lectures on Principles of Medical Imaging, 2016. `https://miac.unibas.ch/PMI/pdf/PMI-01-BasicsOfXray.pdf` accessed on 25.3.2018.

[48] G. F. Knoll, *Radiation Detection and Measurement*. 4th edition, John Wiley & Sons, 2010.

[49] M. Siegbahn. Relations between the K and L Series of the High-Frequency Spectra, *Nature* 96(2416):676, 1916.

[50] F. Zamponi, et. al. Directional Bremsstrahlung from a Ti Laser-Produced X-Ray Source at Relativistic Intensities in the 3–12 keV Range, *Physical review letters*, 105(8):085001, 2010.

[51] E.B. Podgorsak, *Radiation oncology physics: a handbook for teachers and students*. Chaper 1, Vienna: International Atomic Energy Agency, pp. 123-271, 2005.

[52] D. Wu, B. Qiao and X.T. He. The radiation reaction effects in the ultra- intense and ultra-short laser foil interaction regime, *Physics of Plasmas*, 22:093108, 2015.

[53] A. Di Piazza, et.al. Extremely high-intensity laser interactions with fundamental quantum systems, *Reviews of Modern Physics,* 84(3):1177, 2012.

[54] J. Vyskočil, O. Klimo, and S. Weber. Simulations of bremsstrahlung emission in ultra-intense laser interactions with foil targets. *Plasma Physics and Controlled Fusion*, 60(5):05401, 2018.

[55] F. Wan, et. al. Photon emission by bremsstrahlung and nonlinear Compton scattering in the interaction of ultraintense laser with plasmas, *The European Physical Journal D*, 71(9):236, 2017.

[56] O. Klein and Y. Nishina. The scattering of light by free electrons according to Dirac's new relativistic dynamics, *Nature*, 122(3072):398, 1928.

[57] K. V. Lezhnin, et. al. High power gamma flare generation in multi-petawatt laser interaction with tailored targets. *Physics of Plasmas*, 25(12):123105, 2018.

[58] Klein–Nishina formula, Wikipedia, online at `https://en.wikipedia.org/wiki/Klein%E2%80%93Nishina_formula`, accessed on 23.08.2018.

[59] A. Segreto, *et.al.*, Cosmic rays tracks on the PICsIT detector. *Astronomy & Astrophysics*, 411(1), pp. L215-L222, 2003.

[60] U. Amaldi. Fluctuations in calorimetry measurements. *Physica Scripta*, 23(4A), 409, 1981.

[61] B. Rossi. *High Energy Particles*, Prentice-Hall, Inc., Englewood Cliffs, NJ, 1952.

[62] W. R. Nelson, et al. Electron-induced cascade showers in copper and lead at 1 gev, *Physical Review* 149(1):201, 1966.

[63] S. P. Hatchett, et. al. Electron, photon, and ion beams from the relativistic interaction of Petawatt laser pulses with solid targets, *Physics of Plasmas,* 7(5), pp. 2076-2082, 2000.

[64] S. Sakata, et. al. Photonuclear reaction based high-energy x-ray spectrometer to cover from 2 MeV to 20 MeV, *Review of Scientific Instruments*, 85(11):11D629, 2014.

[65] C. D. Chen, et. al. A Bremsstrahlung spectrometer using k-edge and differential filters with image plate dosimeters, *Review of Scientific Instruments*, 79(10):10E305, 2008.

[66] S. Singh, et. al. Compact high energy x-ray spectrometer based on forward Compton scattering for high intensity laser plasma experiments. *Review of Scientific Instruments,* 89(8):085118, 2018.

[67] M. Tanabashi et al. (Particle Data Group). Review of particle physics, *Physical Review D,* 98(3):030001 2018.

[68] C. W. Fabjan and F. Gianotti. Calorimetry for particle physics. *Reviews of Modern Physics*, 75(4): 1243, 2003.

[69] Presentation of Prof. Karl Jakobs, Albert-Ludwigs-Universität Freiburg. Energy measurement in calorimeters, available at: `http://www.particles.uni-freiburg.de/dateien/vorlesungsdateien/particledetectors/kap8`, accessed on 15.9.2018.

[70] G. Gratta, et.al. Crystal calorimeters in particle physics. *Annual Review of Nuclear and Particle Science*, 44(1), pp. 453-500, 1994.

[71] R. Y. Zhu. Radiation damage in scintillating crystals. *Nuclear Instruments and Methods in Physics Research Section A: Accelerators, Spectrometers, Detectors and Associated Equipment*, 413(2-3), pp. 297-311, 1998.

[72] Scintillation counter, Wikipedia, online at `https://en.wikipedia.org/wiki/Scintillation_counter`, accessed on 25.8.2018.

[73] KK Hamamatsu Photonics. *Photomultiplier tubes: Basics and applications.* 3d edition, Chapter 5, 2006.

[74] V. V. Nagarkar, et. al. Fast X-ray/γ-ray imaging using electron multiplying CCD-based detector. Nuclear Instruments and Methods in Physics Research Section A: Accelerators, Spectrometers, *Detectors and Associated Equipment*, 563(1), pp. 45-48, 2006.

[75] S. L. Bugby, L. K. Jambi, and J. E. Lees. A comparison of CsI: Tl and GOS in a scintillator-CCD detector for nuclear medicine imaging, *Journal of Instrumentation,* 11(09):P09009, 2016.

[76] N. Metropolis. The beginning of the Monte Carlo method, *Los Alamos Science*, 15(584): 125-130, 1987.

[77] A. Ferrari, et al. FLUKA: A multi-particle transport code (Program version 2005). No. INFN-TC-05-11, 2005.

[78] G. Battistoni, et al. The FLUKA code: Description and benchmarking, *AIP Conference proceedings*, 896(1), 2007.

[79] V.Vlachoudis. FLAIR: A Powerful But User Friendly Graphical Interface For FLUKA. *Proc. Int. Conf. on Mathematics, Computational Methods & Reactor Physics (M&C 2009), Saratoga Springs, New York*, 2009.

[80] C. Chen, et. al. Bremsstrahlung and Kα fluorescence measurements for inferring conversion efficiencies into fast ignition relevant hot electrons, *Physics of Plasmas*, 16(8):082705, 2009.

[81] C. Zulick, et. al. High resolution bremsstrahlung and fast electron characterization in ultrafast intense laser–solid interactions, *New Journal of Physics,* 15(12):123038, 2013.

[82] General purpose of the EJ-200, EJ-204, EJ-208 and EJ-212 plastic scintillators. ELJEN technology official website online at `https://eljentechnology.com/products/plastic-scintillators/ej-200-ej-204-ej-208-ej-212`, accessed on 1.5.2019.

[83] K. E. Atkinson. *An introduction to numerical analysis,* 2nd edition, John Wiley & Sons, New York, 1989.

[84] M.J. Kim, *et al.*, Characterization of PbWO4 crystals for high-energy physics experiments, *Journal of the Korean Physical Society*, 69(6), pp. 1130-1134, 2016.